# The High Temperature Solubility Limit of Carbon in Alumina

**Li-or Cohen**

# The High Temperature Solubility Limit of Carbon in Alumina

Research Thesis

In Partial Fulfillment of the
Requirements for the Degree of
Master of Science in Materials Science and Engineering

**Li-or Cohen**

Submitted to the Senate of the Technion-Israel Institute of Technology

Shevat 5782 Haifa January 2022

The research thesis was done under the supervision of **Prof. W.D. Kaplan** in the Department of Materials Science & Engineering.

# Acknowledgements

I wish to thank the Technion for partial financial support of this study. This research was partially supported by the Israel Science Foundation (Grant No.1779/18).

I would like to thank Prof. Wayne Kaplan for the inspiration, patience, and constant encouragement.

I would like to thank Dr. Alex Brenner for thought provoking discussion, help and guidance.

I thank to my members friends at the Technion, especially my colleagues in the Metal-Ceramic Interface Group for their support.

Many thanks to my family for their encouragement, love and support.

# Table of Contents

Acknowledgements ..... I

Table of Contents ..... I

List of Figures ..... IV

List of Tables ..... VIII

Abstract ..... 1

List of Symbols and Abbreviations ..... 2

1. Literature Survey ..... 5

1.1 Solid State Sintering ..... 5

1.2 Solubility Limit of Dopants ..... 6

1.2.1 Solute Drag Effect ..... 6

1.2.2 Zener Drag Effect ..... 7

1.3 Alumina ..... 9

1.4 The Influence of Dopants on Alumina ..... 10

1.4.1 MgO Doped Alumina ..... 10

1.4.2 CaO Doped Alumina ..... 10

1.4.3 $SiO_2$ Doped Alumina ..... 11

1.4.4 MgO and CaO Co-Doped Alumina ..... 11

1.4.5 Carbon Doped Alumina ..... 12

1.5 Quantitative WDS measurements ..... 13

1.5.1 Solubility Limit Measurements ..... 17

1.6 The Influence of Sintering Atmosphere on the Solubility Limit of Dopants .. 19

2. Research Goals ..... 21

3. Experimental Methods ..... 22

3.1 Sample Processing ..... 22

3.1.1 The High-Temperature Solubility Limit of Carbon in Alumina ..... 22

3.2 The Influence of Sintering Atmosphere on the High-Temperature Solubility Limit of Mg in Alumina ..... 24
3.3 Characterization ..... 24
3.3.1 Density ..... 24
3.3.2 X-Ray Diffraction ..... 24
3.3.3 Raman Spectroscopy ..... 25
3.3.4 SEM and S/TEM ..... 25
3.3.5 WDS ..... 25
4. Results ..... 27
4.1 The Influence of Carbon on Densification of Alumina ..... 27
4.2 The Solubility Limit of Carbon in Alumina ..... 31
4.2.1 Confirmation of Carbon Saturated Alumina ..... 31
4.2.2 Microstructure and Secondary Carbon Phase Characterization ..... 33
4.2.3 WDS Measurements of Carbon Content ..... 38
4.3 The High-Temperature Solubility Limit of Mg in Alumina ..... 42
4.3.1 Confirmation of Mg Saturated Alumina ..... 42
4.3.2 WDS Measurements of Mg Content ..... 45
4.3.3 WDS Measurements of Carbon Content ..... 45
5. Discussion ..... 46
5.1 The High-Temperature Solubility Limit of Carbon in Alumina ..... 46
5.2 The Influence of Carbon on Densification of Alumina ..... 50
5.3 Carbon Content Measurements ..... 52
5.3.1 Removal of Hydrocarbon Contamination ..... 52
5.3.2 Explanation of the Histogram Shape ..... 53
5.3.3 Possible Errors in the ZAF Correction Applied in this Study ..... 54
5.4 The High-Temperature Solubility Limit of Mg in Alumina ..... 58
6. Summary and Conclusions ..... 60

7. Recommendations for Future Work ..... 61

8. References ..... 63

# List of Figures

Figure 1: Basic phenomena occurring during sintering under the driving force for sintering [1]. ..... 5

Figure 2: Schematic representation of solute drag mechanism in crystalline ceramics. (a) is a symmetrical distribution of the dopant in the region of a stationary grain boundary, (b) is an asymmetric distribution produced by the moving boundary, and (c) is breakaway of the boundary from the dopant leaving a solute cloud behind [3]. ..... 7

Figure 3: (a) Driving force velocity behavior for (a) intrinsic migration (b) solute drag only and (c) total force velocity [5]. ..... 7

Figure 4: Interaction between grain boundary and immobile particle where (a) is an approach of the boundary toward the particle, (b) is the interaction between the grain boundary and the particle, leading to a retarding force on the boundary and (c) is the detailed geometry of the particle–grain boundary interaction [3]. ..... 9

Figure 5: Schematic drawing of the hexagonal (a) and rhombohedral (b) unit cells of α-alumina. The blue spheres represent aluminum cations, and the red spheres represent oxygen anions []. ..... 9

Figure 6: Schematic drawing of the intensity ratio distribution versus WDS measurement location. The interaction volume can intersect grains (and grain boundaries) and can intersect second phase particles (in blue) which will result in a significantly higher signal. ..... 17

Figure 7: Secondary electron SEM micrograph showing an example of a contamination spot (formed in spot-mode in the SEM) and a contamination square (formed by full scan-mode) on the surface of Au coated alumina. ..... 18

Figure 8: Secondary electron SEM micrographs showing the microstructure of sintered carbon doped alumina: (a) thermally etched surface from the cross-section of a sintered sample, and (b) a fracture surface. ..... 30

Figure 9: (a) SE and (b) BSE SEM micrographs of the fracture surface of carbon doped alumina which was doped by infiltration in a 2% glucose solution, which was sintered at 1600°C for 6 hours. (c) and (d) are SE and BSE SEM micrographs of the fracture

surface of the same sample, after heat treatment at 1900°C for 6 hours followed by 6 hours at 1600°C, in a graphite furnace under flowing He. ..... 31

Figure 10: XRD pattern of carbon doped alumina sample, presenting only alumina reflections. Reflections from graphite (or any other phase) were not detected. ..... 32

Figure 11: Representative Raman spectra acquired at a laser wavelength of λ=532 nm from undoped sintered alumina (blue line), and two carbon doped alumina samples (red and black lines). The characteristic carbon peaks D, G, 2D and second order peaks present in the black spectrum indicate the presence of graphite and a carbon content above the solubility limit of carbon in alumina. The absence of carbon characteristic peaks in the red and blue spectra indicates a carbon content below the detection limit of Raman. ..... 33

Figure 12: A bright field TEM micrograph of the 'fully saturated carbon doped alumina' samples (80% relative density). The arrow indicates a secondary phase at the triple junctions. (b) SAD pattern acquired from carbon doped alumina sample. The upper and lower right are simulated electron ring patterns of graphite (red) and alumina (blue)..... 34

Figure 13: STEM-EDS elemental mapping (net intensity) from a representative region of a carbon-doped alumina sample containing both alumina and the secondary phase particle. (a) HAADF-STEM micrograph and (b)-(d) EDS elemental maps of carbon, oxygen and Al. ..... 35

Figure 14: A HAADF-STEM micrograph of an edge-on interface between an alumina grain and a graphite particle. The area delimited with a black square was Bragg-filtered. The {0002} planes of graphite are indicated. The inset shows the FFT from the alumina grain in which $(11\bar{2}0)$ and $(\bar{1}2\bar{1}6)$ planes of alumina are indicated. The $(\bar{1}2\bar{1}6)$ plane is parallel to the interface with graphite, and is marked in the Bragg-filtered region of the STEM micrograph, and the positions of cations in the alumina are indicated by blue dots. ..... 36

Figure 15: (a) ADF-STEM micrograph and (b) EELS spectra of the core-loss carbon-Kα edge from the carbon-doped alumina sample (black spectrum), compared with that of a reference graphite (blue spectrum) and amorphous carbon (red spectrum). The EELS spectra was acquired from the region indicated by a + in (a). The spectrum

from graphite and amorphous carbon were reproduced with permission from [53,54]. ..... 37

Figure 16: (a) WDS measurements of X-ray photons intensity ratio as a function of measurement time, acquired from sintered undoped alumina, Au coated samples, with compression between different days of measurements. (b) A comparison between the X-ray photon intensity ratio measured from sintered undoped alumina and sapphire samples (both Au coated) on the same day of measurements. (c) A comparison between the X-ray photon intensity ratio measured from different spots across a specific sintered undoped alumina sample, on the same measurement day. (d) A SE SEM micrograph of the contamination spot (arrowed). The rectangular contrast is from additional contamination resulting from imaging at a higher magnification (smaller scan-area) before this specific micrograph was acquired. 39

Figure 17: WDS measurements of carbon contamination, measured from an undoped alumina sample (presented as intensity ratio) as a function of the incident electron beam energy. ..... 40

Figure 18: (a) Histogram of the X-ray photon intensity ratio measurements from carbon doped alumina samples rapidly cooled from 1600°C (after removal of the background contamination signal determined on the specific day of measurement and consideration of the Au coating). (b) presents a magnified section of the histogram focusing on the low-intensity ratio regime, which is correlated to X-ray photons emanating from a volume of interaction limited to only carbon saturated alumina (without a signal from the graphitic secondary phase) and converted to carbon concentration using the ZAF correction factor..... 41

Figure 19: Representative Raman spectra acquired at a laser wavelength of λ=532 nm from undoped alumina sintered in air (black line), gray alumina, which is an undoped alumina sample sintered in a graphite furnace, under flowing He (blue line) and carbon doped alumina (red line). No observation of carbon characteristic peaks indicates a carbon content below the detection limit of Raman..... 42

Figure 20: XRD pattern confirming the presence of alumina, and binary and ternary phases, thus ensuring saturation of the alumina grains with Mg. ..... 43

Figure 21: Representative Raman spectra acquired at a laser wavelength of λ=532 nm from undoped alumina (black line), and Mg doped alumina sample sintered in air and

annealed at 1600C for 20 h at a relatively low oxygen partial pressure, in a graphite furnace, under flowing He (blue line). The absence of carbon characteristic peaks in the spectra indicates a carbon content below the detection limit of Raman. ..... 44

Figure 22: A SE SEM micrograph of the fracture surface of a Mg doped alumina sample sintered in air and annealed for 20 h at a relatively low oxygen partial pressure. The sample had a 95% relative density. ..... 44

Figure 23: (a) Histogram of the Mg-Kα X-rays photon measurements from Mg doped alumina samples annealed at a relatively low oxygen partial pressure and rapidly cooled from 1600°C. (b) is a magnified section of the histogram focusing on the low intensity ratio regime, which is correlated to X-ray photons emanating from a volume of interaction limited to only Mg saturated alumina, without a signal from the Mg spinel secondary phase (the first peak) and from the overlap with grain boundaries (the second peak). ..... 45

Figure 24: A Monte-Carlo simulation for 500 electron trajectories through Au assuming 10 kV incident beam. The trajectories in red indicate backscattered electrons that eventually escape from the surface of the sample. The simulation was calculated using the software program Casino [73]. ..... 55

Figure 25: A schematic drawing of the interaction volume in alumina under a 10 nm thick Au coating. A conservatively large beam diameter of 500nm was used to estimate the total number of Au atoms hypothetically dissolved in the interaction volume. From this the possible influence of Au fluorescence was estimated. ..... 56

Figure 26: A Monte-Carlo simulation for 500 electron trajectories at 10 kV incident energy through (a) alumina with a 10 nm Au coating and (c) alumina without a coating, and the carbon-Kα distribution in (b) Au coated alumina and (d) non-coated alumina. The distributions are separated to absorbed (red) and non- absorbed (blue) carbon-Kα [73]. ..... 57

# List of Tables

Table 1: The influence of carbon on densification of alumina. ..... 27

Table 2: The possible reaction in the sintering system, the standard state Gibbs free energies of them and the required oxygen partial pressure of each reaction. ..... 49

# Abstract

The solubility limit of carbon in 99.99% pure $\alpha$-$Al_2O_3$ (alumina) equilibrated at 1600°C under flowing He in a graphite furnace (which correlates to a relatively low oxygen partial pressure) was measured using a wavelength dispersive spectrometer mounted on a scanning electron microscope. Undoped alumina and alumina containing carbon at a concentration resulting in the precipitation of a second phase were prepared and equilibrated at 1600°C. The undoped alumina samples were used to quantify the amount of carbon deposited on the surface of samples because of hydrocarbon contamination in the electron microscope, and this background level was removed from the signal measured from carbon-doped samples. The solubility limit of carbon in alumina was found to be 3940 ± 906 ppm with a detection limit of 15 ppm, and it is believed that carbon substitutes oxygen as an anion and this is charge-compensated by the formation of oxygen vacancies. Below the solubility limit carbon does not hinder densification and limits grain growth. Above the solubility limit carbon hinders densification.

In addition, the solubility limit of Mg in alumina at a relatively low oxygen partial pressure was measured in order to study the influence of oxygen partial pressure on the solubility limit of dopants (Mg in this case) in alumina. The solubility limit of Mg in alumina at a relatively low oxygen partial pressure was found to be 166± 42 ppm at 1600°C.

# List of Symbols and Abbreviations

| | |
|---|---|
| $r_K$ | Absorption edge jump of K shell |
| $E_a$ | Activation energy |
| ADF | Annular dark field |
| Z | Atomic number |
| $\langle x \rangle$ | Average distance travelled by a diffusing particle in a certain time |
| $I_{bgd}$ | Background intensity |
| BSE | Backscattered electrons |
| $C_\infty$ | Bulk solute concentration |
| $°C$ | Celsius degrees |
| $C_{std}$ | Concentration of element of interest in the standard |
| $[X]$ | Concentration of element X |
| $C$ | Concentration of the element of interest |
| $g_{ZAF}$ | Correction factor for atomic number, absorption, and fluorescence |
| $\delta$ | Corresponding ratio for continuum fluorescence contribution |
| $E_c$ | Critical excitation energy |
| $\rho$ | Density |
| DFT | Density functional theory |
| $\delta r$ | Difference between the radius of the solvent and solute |
| $D$ | Diffusion coefficient |
| $D_o$ | Diffusion constant |
| $\psi$ | Dihedral angle |
| $\beta$ | Drift velocity |
| $F_b$ | Driving force per unit area for boundary motion |
| $D$ | Dry weight |
| EELS | Electron energy loss spectroscopy |
| EDS | Energy dispersive spectroscopy |
| $K_P$ | Equilibrium constant of a certain reaction |
| $\omega_k$ | Fluorescence yield of the K shell X-rays photons |

| | |
|---|---|
| $R$ | Gas constant |
| $\alpha$ | Geometrical shape factor |
| $\Delta G_T^\circ$ | Gibbs free energy at standard state of a certain temperature |
| $\gamma_{GB}$ | Grain boundary energy |
| $V_{GB}$ | Grain boundary velocity |
| $G$ | Grain size |
| $C_p$ | Heat capacity |
| $\Delta a,\ \Delta b,\ \Delta c$ | Heat capacity constants |
| HAADF | High Angle Annular Dark Field |
| HAADF | High angle annular dark field |
| HRTEM | High resolution transmission electron microscopy |
| $h$ | Hour |
| $E_0$ | Incident electron energy |
| I | Integration constant |
| $\Delta H_0$ | Integration constant |
| $F_0$ | Intrinsic drag |
| $C_{\mathrm{lim},0.95}$ | Limit of detection (at a confidence larger than 95%) |
| $\left(\mu/\rho\right)$ | Mass absorption coefficient |
| $\Delta\rho z$ | Mass-thickness |
| $\phi\left(\Delta\rho z\right)$ | Mass-thickness distribution |
| $\tau$ | Measurement time |
| $M$ | Molar mass |
| $m$ | Number of measurements |
| $I_0$ | Original X-ray intensity |
| $P_{O_2}$ | Oxygen partial pressure |
| $P$ | Pressure |
| $r$ | Radius |
| $\sigma$ | Ratio between the intensity of fluorescence emission and the primary characteristic X-ray emission |

| | |
|---|---|
| $k$ | Ratio of intensity of characteristic X-ray radiation measured from the sample to that measured from the standard |
| $F_r$ | Retarding force |
| $W$ | Saturated weight |
| SEM | Scanning electron microscopy |
| STEM | Scanning transmission electron microscopy |
| SE | Secondary electrons |
| SIMS | Secondary ion mass spectrometry |
| SAD | Selected area diffraction |
| $\mu$ | Shear modulus |
| $F_s$ | Solute drag |
| $\alpha_s$ | Solute drag force per unit velocity per unit solute concentration |
| $\delta\varepsilon$ | Strain energy associated with a single solute atom |
| $\Gamma$ | Surface or interface energy |
| $S$ | Suspended weight |
| $T$ | Temperature |
| $\Delta G^\circ$ | The change in Gibbs free energy at standard state |
| $\Delta H_T^\circ$ | The change in standard stat enthalpy at certain temperature |
| $x$ | Thickness |
| $t$ | Time |
| $A$ | Total interface area |
| TEM | Transmission electron microscopy |
| WDS | Wavelength dispersive X-ray spectroscopy |
| XRD | X-ray diffraction |
| $I_F$ | X-ray intensity due to fluorescence |
| $\theta$ | X-ray take-off angle |
| $I$ | X-rays intensity |
| $k$ | X-rays intensity ratio |
| $Z_r$ | X-rays interaction depth |
| $d$ | X-rays interaction diameter |

# 1. Literature Survey

## 1.1 Solid State Sintering

The manufacturing of ceramics is done by sintering since it is difficult to reach temperatures above the melting point of most ceramic materials. Sintering is usually carried out at a temperature of $0.5T_m<T<0.8T_m$ which enables sufficient atomic mobility. The driving force for sintering is the reduction of the total surface/interfacial energy of the system [1]:

$$\Delta(\gamma A) = \Delta\gamma A + \gamma\Delta A \tag{1}$$

where $\gamma$ is the total surface/interfacial energy, $A$ is the total interface area and $\gamma A$ represents the total interfacial energy of a powder compact. The change in total surface energy $\Delta\gamma$ is due to densification, while the change in interfacial area $\Delta A$ is due do grain growth/grain coarsening. Densification and coarsening are competitive processes that can occur simultaneously, as presented schematically in Figure 1.

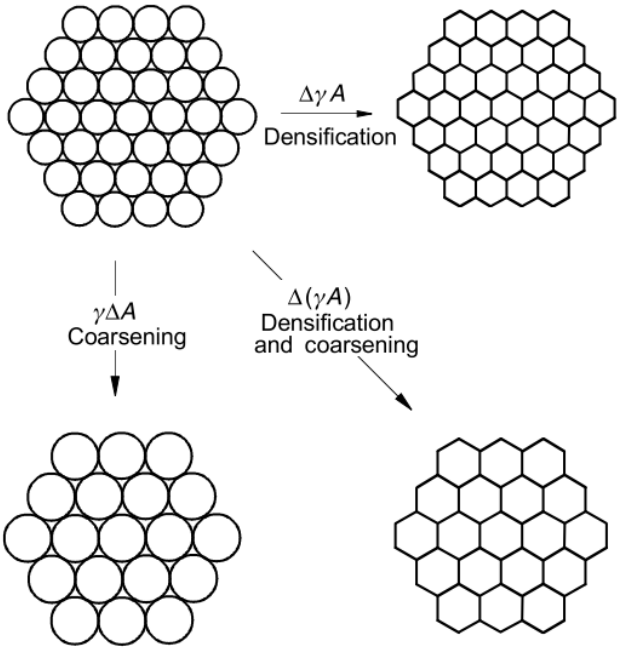


Figure 1: Basic phenomena occurring during sintering under the driving force for sintering [1].

When densification is the main process during sintering, a reduction of pore size will occur and the density will increase. When coarsening is dominant, pore and particle growth will occur. According this simple concept, controlling sintering is a one of the biggest challenges in the ceramic industry.

## 1.2 Solubility Limit of Dopants

One way sintering can be controlled is by doping. Impurities or dopants in a polycrystalline material can influence grain boundary mobility (the normalized velocity of grain boundaries), densification rates, mechanical and functional properties, optical properties, etc. It is convenient to examine the role of dopants/impurities at concentrations *below* the solubility limit versus concentrations *above* the solubility limit. The solubility limit is the analytical composition of a saturated solution, expressed in terms of the proportion of a designated solute in a designated solvent. The solubility may be expressed as a concentration, molality, mole fraction, mole ratio, etc. [2].

### 1.2.1 Solute Drag Effect

Equilibrium (Gibbsian) segregation of solute atoms to grain boundaries can occur, driven by a reduction in grain boundary energy. In this case, the solute can have interaction (attraction or rejection) with the grain boundary due to an interaction potential, and the solute ions will tend to have a non-uniform distribution at the grain boundary. Figure 2(a) presents a schematic drawing of a symmetric solute (ionic) distribution at a grain boundary which is self-compensated via a space charge. In Figure 2(b) the grain boundary starts to move and an asymmetric solute profile occurs since the diffusivity of the solute ions across the boundary is expected to be different from that of the host. This asymmetry results in a drag force (solute drag $F_s$) on the boundary which reduces the mobility. If the driving force for boundary migration is large enough, the boundary can break away from the high concentration of solute (often described as a solute cloud) as shown in Figure 2(c) [3].

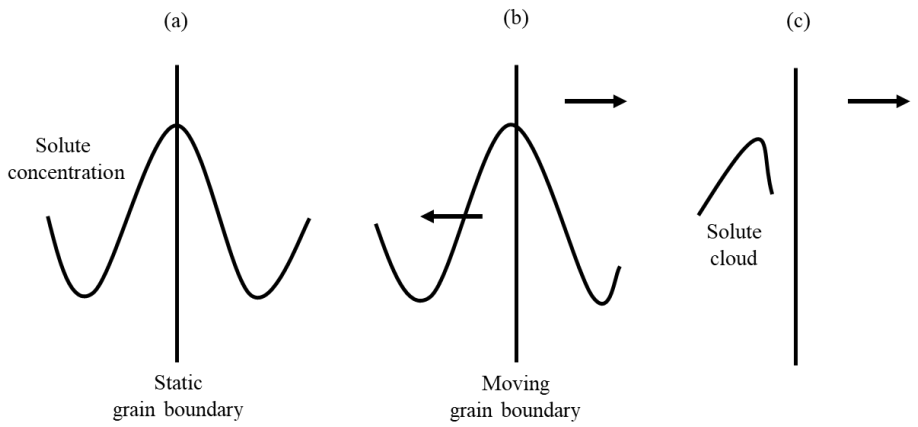

Figure 2: Schematic representation of solute drag mechanism in crystalline ceramics. (a) is a symmetrical distribution of the dopant in the region of a stationary grain boundary, (b) is an asymmetric distribution produced by the moving boundary, and (c) is breakaway of the boundary from the dopant leaving a solute cloud behind [3].

Cahn was the first to calculate the solute drag force $F_S$ [4]:

$$F_S = \frac{\alpha C_\infty V_{GB}}{[1+\beta V_{GB})^2]} \tag{2}$$

where $\alpha$ is the solute drag force per unit velocity per unit solute concentration in the low velocity limit, $C_\infty$ is the bulk solute concentration, $V_{GB}$ is the grain boundary velocity and $\beta^{-1}$ is the drift velocity with which a solute diffuses across the grain boundary region. In steady state, the total drag force is assumed to be the sum of intrinsic drag force $F_0$ and the solute drag force, as shown in Figure 3 [5].

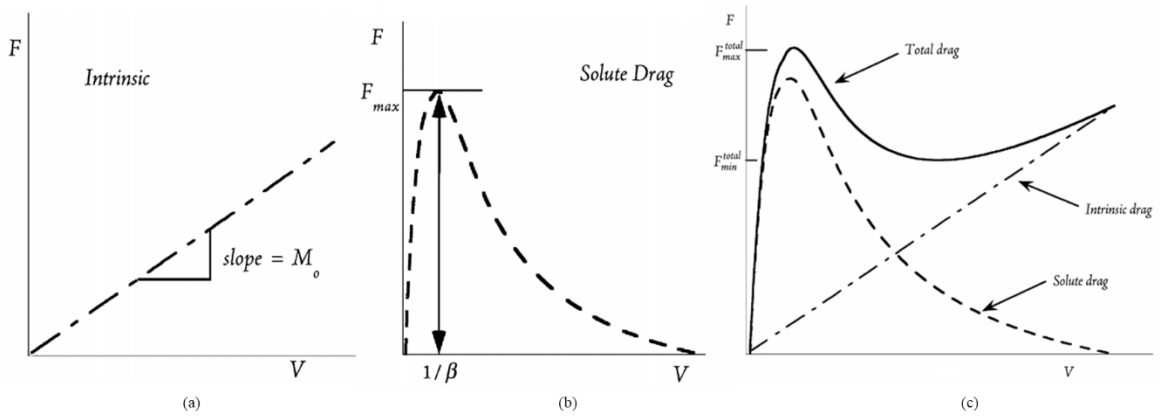


Figure 3: (a) Driving force velocity behavior for (a) intrinsic migration (b) solute drag only and (c) total force velocity [5].

This model explains the decrease in grain boundary mobility when a solute is introduced to the system. However, this model is does not explain the solute acceleration phenomena, when an increase in grain boundary mobility occurs.

### 1.2.2 Zener Drag Effect

When the dopant/impurity concentration is above the solubility limit, precipitation in the form of second phase particles will occur according to the phase diagram. The first quantitative model to describe particle inhibited grain growth was developed by Zener [3]. Zener assumed that the particles have a spherical shape, they are insoluble, immobile, and randomly distributed

in the polycrystalline solid. By taking a grain boundary with principal radii of curvature, the driving force per unit area for boundary motion is:

$$F_b = \gamma_{GB}\left(\frac{1}{a_1}+\frac{1}{a_2}\right) \tag{3}$$

where $F_b$ is the driving force, $\gamma_{GB}$ is the grain boundary energy and $a_1$ and $a_2$ are the radii of curvature.

Assuming that $a_1$ and $a_2$ are proportional to the grain size $G$, then

$$F_b = \frac{\alpha\gamma_{GB}}{G} \tag{4}$$

where $\alpha$ is a geometrical shape factor.

When the grain boundary intersects an inclusion, as presented in Figure 4, its movement is hindered and a retarding force acts on the boundary:

$$F_r = \left(\gamma_{GB}\cos\psi\right)(2\pi r\sin\psi) \tag{5}$$

where $F_r$ is the retarding force, $r$ is the radius of the inclusion and $\psi$ is the dihedral angle.

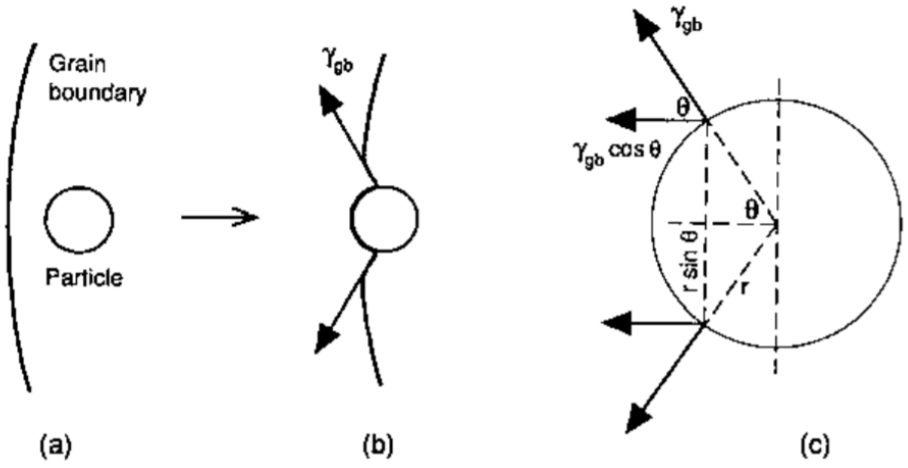

Figure 4: Interaction between grain boundary and immobile particle where (a) is an approach of the boundary toward the particle, (b) is the interaction between the grain boundary and the particle, leading to a retarding force on the boundary and (c) is the detailed geometry of the particle–grain boundary interaction [3].

In order to study and understand the mechanisms by which impurities or dopants affect the microstructure (solute drag or Zener drag), and by that to control the changes in the ceramic properties due to doping, the solubility limit of the dopant in the doped system must be known.

## 1.3 Alumina

Alumina ($Al_2O_3$) has several metastable structures, where α-alumina (corundum form) is the thermodynamically stable structure of alumina [6]. α-alumina possesses a trigonal symmetry with rhombohedral Bravais centering (space group $R\bar{3}c$ (No. 167)) and has 10 atoms in the unit cell. However, it is common to represent α-alumina using a hexagonal unit cell, which following Kronberg contain 30 atoms; 18 aluminum atoms and 12 oxygen atoms (see Figure 5) [7].

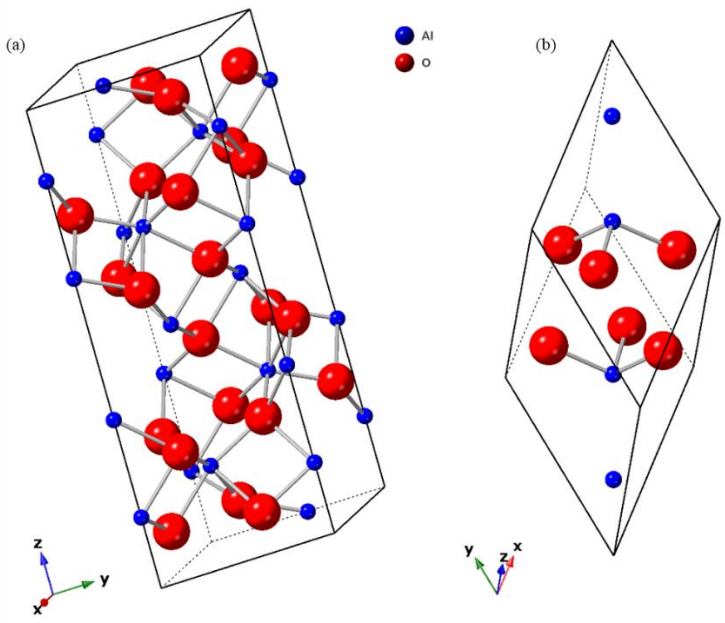


Figure 5: Schematic drawing of the hexagonal (a) and rhombohedral (b) unit cells of α-alumina. The blue spheres represent aluminum cations, and the red spheres represent oxygen anions [8].

Alumina is one of the most studied ceramic systems, mostly due to its application in corrosive environments, resistance to abrasion, reasonable fracture strength, etc.

## 1.4 The Influence of Dopants on Alumina

### 1.4.1 MgO Doped Alumina

When the ceramic industry started to use alumina, a lack of densification after processing occurred. Coble was the first to reach full density to alumina, by doping it with MgO [9]. He sintered Mg-doped alumina under hydrogen and by that he developed translucent polycrystalline alumina for high-pressure sodium lamps. Afterwards, Mg was found to minimize abnormal grain growth and reduce grain boundary mobility and grain size as a result [10,11,12].

The phase diagram of alumina and MgO does not contain a solubility field of MgO in alumina [13]. Roy and Coble reported 300 ppm as the solubility limit of MgO in alumina at 1630°C [11]. However, no determination of the actual Mg concentration after sintering was done in this work. Miller et al. studied the solubility limit of MgO in alumina at 1600°C using quantitative wavelength dispersion spectroscopy (WDS) and measured it to be 132 ± 11 ppm [14].

With the knowledge of the solubility limit of MgO in alumina, the influence of MgO on grain boundary mobility of alumina could be determined. Akiva et al. studied the influence of Mg on the mobility of alumina, at a Mg concentration which was experimentally confirmed to be below the solubility limit, and demonstrated a decrease in grain boundary mobility due to the solute drag effect [15].

### 1.4.2 CaO Doped Alumina

In contrast to MgO, doping alumina with CaO was found to increase grain growth and grain boundary mobility, by accelerating grain boundary movement [16,17]. However, without the knowledge of the solubility limit, one cannot distinguish whether equilibrium segregation or precipitation of a second phase occurred and caused the increased grain boundary mobility. Similar to MgO, there is no solubility range for CaO in alumina in the published phase diagram of alumina and CaO [18]. Akiva et al. measured the solubility limit of CaO in alumina at 1600°C using the same WDS technique that Miller et al. developed, and found it to be 51 ± 1 ppm [14,19]. Afterwards, the solubility limit of CaO in alumina was measured at 1500°C and 1400°C, and the solubility limit range in the CaO-alumina phase diagram was published [20]. After the high temperature solubility limit of CaO in alumina was measured, it was

experimentally proven by Akiva et al. that doping alumina with CaO below the solubility limit resulted in increased grain boundary mobility [15].

### 1.4.3 $SiO_2$ Doped Alumina

Doping alumina with Si results in increased grain growth. Bae and Baik doped alumina with Si and reported abnormal grain growth due to the formation of a liquid phase [21]. They determined that doping alumina with Si above 300 ppm will cause abnormal growth to occur, and compared this with the solubility limit (300 ppm at 1600°C) determined by Lee and Kröger (by electrical conductivity measurements). Dillon and Harmer correlated Si concentration with abnormal grain growth and reported on an adsorption transition together with a change in grain growth kinetics [22]. However, no determination of the actual Si concentration after sintering was done in both studies, and without knowledge of the solubility limit, the mechanism by which Si affects the microstructure is unknown.

As well as MgO and CaO, the published phase diagram of alumina and $SiO_2$ does not include a solubility range of $SiO_2$ in alumina [23]. Moshe et al. determined the solubility limit of $SiO_2$ in alumina at 1600°C, using fully standardized WDS, to be 188 ± 7 ppm [24].

### 1.4.4 MgO and CaO Co-Doped Alumina

Co-doped alumina systems have been studied as well. Handwerker et al. studied the influence of Mg on grain growth of alumina together with the influence of Ca and Si [25]. They hypothesized that Mg may increase the solubility limit of impurities, such as Ca and Si, preventing the formation of secondary liquid phases which may increase the rate of grain growth. The influence of Mg on Ca (and vacancies) on alumina was studied by determining the solubility limits of Mg and Ca in a system that contains them both [26]. It resulted in a decrease in the Ca solubility limit due to Mg, and an increase in the solubility limit of Mg in alumina due to presence of Ca. These results indicate that Mg and Ca co-doped alumina resulted in a higher Mg concentration in the grains, compared to Mg doped alumina, and the amount of Mg excess to exert a solute-drag force on alumina grain boundaries should also increase, resulting in a decreased grain boundary mobility.

### 1.4.5 Carbon Doped Alumina

The present work focuses on the carbon doped alumina system. Alumina is commonly sintered in air, but several sintering techniques require protection from oxidation and good electrical conduction, such as spark plasma sintering (SPS) and flash sintering, where a graphite die is often used [27,28]. As a result, the potential influence of carbon on the microstructural evolution of alumina is of interest.

The influence of carbon on sintering and microstructural evolution of alumina has been addressed in the past. Michalek et al. studied the influence of carbon on sintering alumina in different environments and demonstrated that under relatively low oxygen partial pressure ($P_{O_2}$) (vacuum sintering) carbon prevented densification and grain growth [29]. Yahya et al. studied the influence of small amounts of carbon (120 ppm) on the fracture mode and wear resistance of alumina, and demonstrated that doping alumina with carbon resulted in a change of fracture mode to transgranular fracture and a correlated increase in wear resistance [30]. This could be attributed to carbon adsorption to grain boundaries in alumina, which was previously demonstrated by Marquis et al. using atom probe tomography [31]. Marder et al. showed a significant influence of carbon on the grain size of alumina, resulting in smaller grains and an increase in wear resistance [32]. They also reported a decrease in the relative density as a result of doping with ~3 wt.% of carbon. On the other hand, when they sintered undoped alumina in a graphite furnace, the density did not change compared to undoped alumina (sintered in air), and there was no second phase. By that they concluded that the amount of doping from the graphite furnace was below the solubility limit, and correlated to solute drag. Miranzo et al. examined the influence of sintering environment on densification and electrical properties of alumina [33]. Their samples were sintered in air or in a $CO/CO_2$ atmosphere, and sintering in a $CO/CO_2$ atmosphere resulted in a lower density, which was explained by the presence of carbon.

In addition to sintering and microstructural evolution, several studies have investigated the influence of carbon on the properties of alumina. Miranzo et al. also demonstrated a change in electrical properties due to the sintering atmosphere and the presence of carbon [33]. Ahmad et al. studied the mechanical properties of hot-pressed carbon nanotube (CNT) reinforced alumina and demonstrated that adding carbon nanotubes up to a concentration of 4 vol.% increased the fracture toughness, hardness, and flexural strength, while carbon nanotube

concentrations of 10 vol.% resulted in a decrease in mechanical properties [34]. More studies have focused on the influence of carbon on optical properties, including changes in color centers and improvement in the thermoluminescence (TL) sensitivity of alumina due to carbon doping [35,36,37,38,39,40].

It is clear that carbon can have a significant influence on the microstructure and properties of alumina, and it is important to correlate the actual carbon concentration with microstructural changes. To understand the mechanism by which carbon affects grain growth of alumina, by adsorption (solute drag or solute acceleration) or by drag induced by a secondary phase (Zener drag), it is important to know the solubility limit of carbon in alumina at the processing temperature, and by that to control the microstructure and the final properties. Futazuka et al. conducted simulations to predict the preferred mechanism and correlated energy of point defects associated with impurity ions in doped-alumina systems [41]. Their simulations, similar to Zhu et al [40], indicated that in a low oxygen pressure, carbon behaves as an anion and replaces oxygen anions, and produces oxygen vacancies as a charge compensating mechanism. According to Futazuka's calculations, the solubility limit of carbon in alumina should be ~$4 \cdot 10^{-5}$ ppm.

To the best of the authors' knowledge, the solubility limit of carbon in alumina at temperatures and oxygen partial pressures relevant to sintering has not been measured.

## 1.5 Quantitative WDS measurements

As mentioned before, the high temperature solubility limit of other key dopants/ impurities in alumina have been measured using quantitative wavelength dispersion spectroscopy (WDS) [14,19,20,24,26]. To obtain quantitative WDS data, the measured intensity of a particular characteristic X-ray line from the sample is compared with that from a reference standard of known composition. This approach was first proposed by Castaing in his pioneering work on the subject in 1951. Hence by keeping the instrumental settings (kV, beam current, X-ray spectrometer) constant while the X-ray intensity readings are acquired, such factors as spectrometer efficiency are eliminated from the calculation and we must consider only the different electron and X-ray behavior in the sample and the standard [42].

For a binary sample containing elements A and B, the mass concentration of A can be determined by reference to a standard consisting of the pure element A. The intensity of the primary X-ray emission is given by [42]:

$$I = \phi(\Delta\rho z)\int_0^{\infty} \phi(\Delta\rho z)\exp(-\chi\rho z)\,\mathrm{d}\rho z \tag{6}$$

and:

$$\chi = \left(\mu/\rho\right)\cdot \mathrm{cosec}(\theta) \tag{7}$$

where $I$ is X-ray intensity, $\phi(\Delta\rho z)$ is the mass-thickness distribution corresponding to the emission from an isolated thin film of mass thickness $\Delta\rho z$, $\left(\mu/\rho\right)$ is the mass absorption coefficient and $\theta$ is the X-ray take-off angle towards the detector.

The total emitted X-ray intensity including any florescence contribution in then:

$$I = \phi(\Delta\rho z)\int_0^{\infty} \phi(\Delta\rho z)\exp(-\chi\rho z)\,\mathrm{d}\rho z\ (1+\sigma+\delta) \tag{8}$$

where σ is the ratio of the intensity of fluorescence emission to the primary characteristic X-ray emission, and δ is the corresponding ratio for continuum fluorescence contribution. Equation (8) can be rewritten as:

$$I = \phi(\Delta\rho z)\int_0^{\infty} \phi(\Delta\rho z)\,\mathrm{d}\rho z\ f(\chi)(1+\sigma+\delta) \tag{9}$$

where:

$$f(\chi) = \frac{\int_0^{\infty} \phi(\Delta\rho z) \exp(-\chi\rho z)\, \mathrm{d}\rho z}{\int_0^{\infty} \phi(\Delta\rho z)\, \mathrm{d}\rho z} \tag{10}$$

The ratio of x-ray intensities (A radiation) emitted from specimen AB and standard A is then:

$$\frac{I_A^{AB}}{I_A^A} = \frac{\phi(\Delta\rho z)_A^{AB}}{\phi(\Delta\rho z)_A^A} \frac{\left[\int_0^{\infty} \phi(\Delta\rho z)\, \mathrm{d}\rho z\right]_A^{AB}}{\left[\int_0^{\infty} \phi(\Delta\rho z)\, \mathrm{d}\rho z\right]_A^A} \frac{f(\chi)_A^{AB} \cdot (1+\sigma+\delta)_A^{AB}}{f(\chi)_A^A \cdot (1+\sigma+\delta)_A^A} \tag{11}$$

Now it may be shown as follows that:

$$C_A = \frac{\phi(\Delta\rho z)_A^{AB}}{\phi(\Delta\rho z)_A^A} \tag{12}$$

where $C_A$ is the mass concentration of element A in specimen AB.

The integral terms correspond to the areas under the respective $\phi(\Delta\rho z)$ curves and their ratio is referred to as the atomic number correction factor **Z**. The $f(\chi)$ ratio may be replaced by **A** to denote the absorption correction factor and the **F** factor instead of the fluorescence ratio terms. By that, equation (12) can be rewritten as:

$$\frac{I_A^{AB}}{I_A^A} = g_{ZAF} \cdot C_A \tag{13}$$

where $I_A^{AB}$ is the X-ray photons intensity of element A in specimen AB and $I_A^A$ is the x-ray photons intensity of element A in standard specimen A and $g_{ZAF}$ is the atomic number (Z), absorption (A) and fluorescence (F) correction factor (ZAF correction factor). The concentration can be determined using [43]:

$$C = k \cdot g_{ZAF} \cdot C_{std} \tag{14}$$

where $C_{std}$ is the concentration of the element of interest in the standard and $k$ is the X-ray photons intensity ratio $\frac{I_A^{AB}}{I_A^A}$.

During any quantitative analysis, the detection limit needs to be measured as well. The detection limit of the element of interest in the matrix can be experimentally determined using [43]

$$C_{\lim,0.975} = g_{ZAF} \cdot \frac{2\sqrt{2I_{bgd}}}{\sqrt{m\tau} I_{std}} \tag{15}$$

where $C_{\lim,0.975}$ is the limit of detection (at a confidence larger than 975%), $m$ is the number of measurements, $\tau$ is the measurement time, $I_{bgd}$ is the background intensity measured in the sample, and $I_{std}$ is the intensity from a standard with a known concentration.

The depth of penetration can be estimated from [42]

$$Z_r = \frac{0.033M(E_0^{1.7} - E_c^{1.7})}{\rho Z} \tag{16}$$

where $Z_r$ is the interaction depth, $E_0$ is the incident electron energy, $E_c$ is the critical excitation energy, ρ is the density of the matrix, $M$ and $Z$ are the atomic weight and atomic number of the element of interest respectively.

The diameter of the interaction volume $d$ can be expressed as [42]

$$d = \frac{0.077(E_0^{1.5} - E_c^{1.5})}{\rho} \tag{17}$$

### 1.5.1 Solubility Limit Measurements

The approach used in this work is to obtain a distribution of the concentration of the element of interest (the dopant) that can be divided into two main regions, as shown in Figure 6. The first region, which is related to the low concentration region, corresponds to the dopant concentration within the alumina grains, which is the solubility limit if a secondary phase exists in the equilibrated microstructure. The second region corresponds to the dopant concentration of the second phase particles that reside within the interaction volume, and dopant from the alumina grains. There are cases which a third region can be discerned, which is an intermediate region because of overlap of the electron probe (and interaction volume) between the regions of the alumina grains and the secondary phase, and because of the possible contribution of the dopant segregated at grain boundaries.

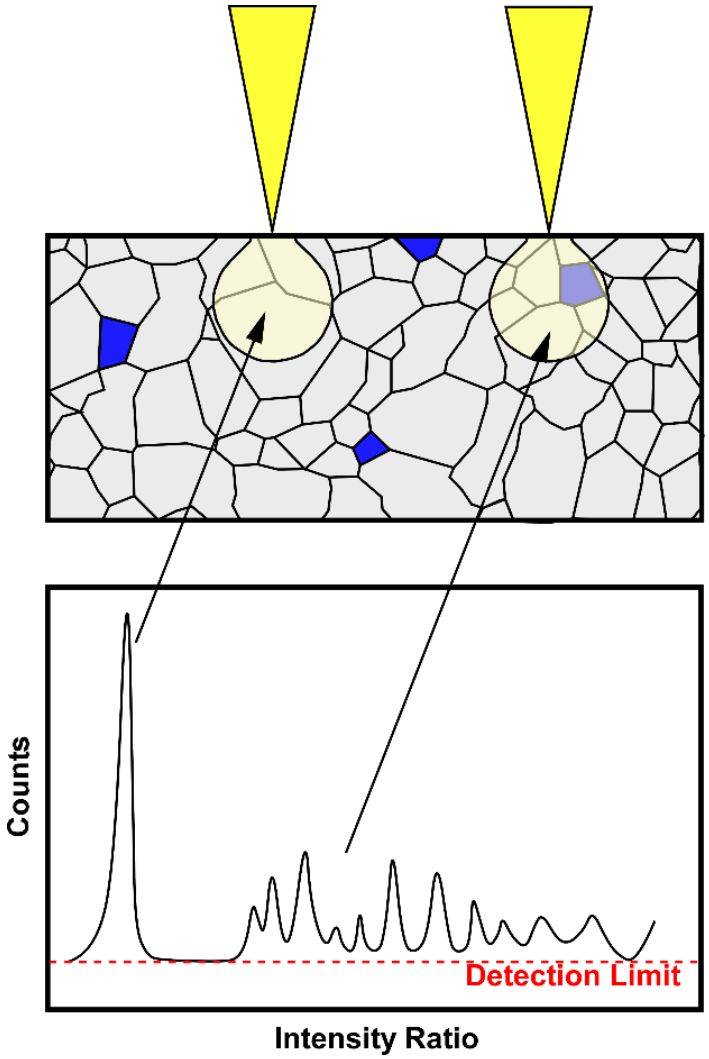


Figure 6: Schematic drawing of the intensity ratio distribution versus WDS measurement location. The interaction volume can intersect grains (and grain boundaries) and can intersect second phase particles (in blue) which will result in a significantly higher signal.

After the intensity measurements, the dopant concentration can be determined by calculation of the relevant ZAF correction factor use of Eq (14). These values of concentration can only be determined for intensities measured from regions without secondary phases, i.e. the low intensity ratio region of Figure 6 (since the ZAF correction factor is relevant only for a one-phase system).

#### 1.5.1.1 Carbon Content Measurements

The problem with this method applied to carbon in alumina, is the ubiquitous formation of carbon hydrocarbon contamination in the electron microscope. In general, hydrocarbon contamination on the surfaces of electron microscopy specimens is unavoidable. During any SEM/TEM observations formation of carbon contamination in the electron microscope occurs, due to cracking of hydrocarbons bonds (-CH, -COOH, -$CNH_2$, and other bonds) adsorbed to the surface of the sample (and stage and chamber) [44,45]. The result is polymerization by cross-linking, and a carbon-rich contamination area grows over the scanned area. The irradiated area usually appears darker in the SEM/TEM micrographs and is normally a square or spot with a diameter nearly equal to that of the illumination region. Figure 7 presents an example of contamination during SEM. The contamination layer may also cover underlying structures and this decreases the resolution [45].

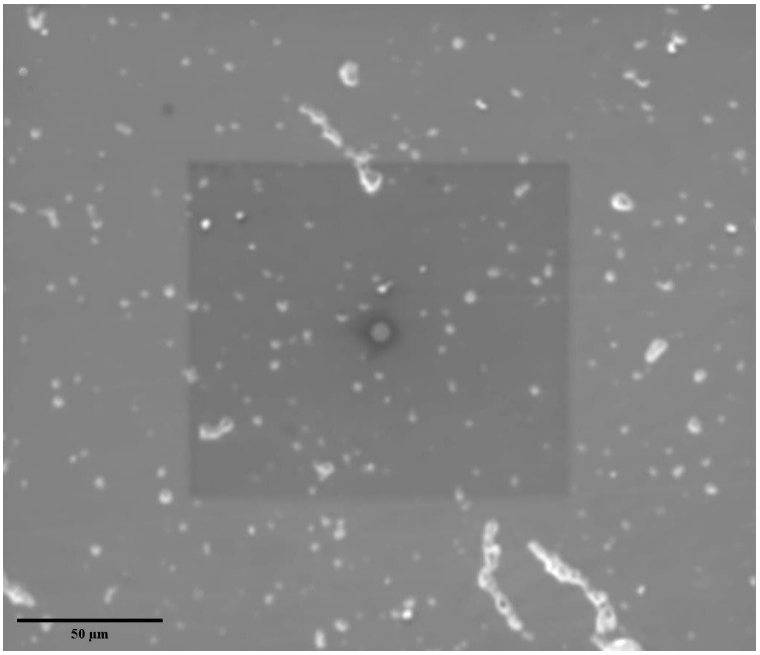


Figure 7: Secondary electron SEM micrograph showing an example of a contamination spot (formed in spot-mode in the SEM) and a contamination square (formed by full scan-mode) on the surface of Au coated alumina.

Generally, sources of hydrocarbon contamination in the electron microscope can be attributed to one or a combination of the major contributors: (1) the pumping system, where electron microscopes equipped with diffusion and/or rotation pumps are often considered to be inherently "dirty" pumping systems; (2) outgassing of other internal SEM component parts (sample stage, stage lubricants, etc.); and/or (3) the history of the sample (including its preparation and handling) and the nature of the sample (degree of hydrocarbon adhesion to it) [46].

Specimen and electron microscope contamination can be minimized, but are difficult to fully avoid. Even ultra-high vacuum will not entirely prevent hydrocarbon contamination, since hydrocarbons can deposit on the specimen surface prior to its entry into the microscope. Various solutions for monitoring and reducing sample contamination have been reported, such as sample heating prior/during observation, various cleaning procedures (e.g. plasma etching), and using cold-traps in order to reduce the partial pressure of hydrocarbons (and other gases) near the sample [45,46].

Hydrocarbon contamination obviously means an additional carbon signal. This must be considered during any quantitative carbon measurements, including the carbon solubility limit measurements discussed here. As such, one of the goals of the present work was to develop a WDS-based method for the measurement of carbon concentration which considers carbon contamination, and to thus determine the solubility limit of carbon in alumina.

## 1.6 The Influence of Sintering Atmosphere on the Solubility Limit of Dopants

For alumina, past measurements of solubility limits have been mostly limited to samples equilibrated in air (a relatively high oxygen partial pressure). According to Futazuka et al., the solubility limit of group IIA (including Mg and Ca) should not be significantly affected by the oxygen partial pressure [41]. However, for the case of group VI elements (including Si and carbon), the oxygen partial pressure should influence the solubility limit (in the case of carbon due to the tendency to produce $CO/CO_2$) [41]. Hollenberg et al. studied the influence of the oxygen partial pressure on the creep of Fe, Cr and Ti doped alumina systems [47]. They reported an increase in creep rate with an increase in the oxygen partial pressure for Ti doped alumina, in contrast to Fe doped alumina samples which showed a decrease in creep rate with increase

in the oxygen partial pressure. For the case of Cr doped alumina, the oxygen partial pressure did not influence the creep rate. It was concluded that the oxygen partial pressure changes the defect chemistry of the Fe doped and Ti doped alumina systems.

# 2. Research Goals

The main goal of this research was to determine the high-temperature (1600°C) solubility limit of carbon in alumina, and by that to understand the concentration dependent influence of carbon on microstructural evolution of alumina. A secondary goal was to determine the high temperature solubility limit of Mg in alumina at 1600°C at a low oxygen partial pressure, for comparison with the values reported for high oxygen partial pressure [14].

# 3. Experimental Methods

In this section alumina processing routes, characterization methods and methodology will be presented.

## 3.1 Sample Processing

### 3.1.1 The High-Temperature Solubility Limit of Carbon in Alumina

#### 3.1.1.1 Undoped Alumina

Polycrystalline alumina samples were prepared using 100 gr of high purity (99.99%) $\alpha$-$Al_2O_3$ powder (Ceralox HPA 0.5, Tucson, AZ), 65 gr of distilled water, and deflocculated with a small amount of HCl to reach a pH of ~4 to prevent agglomeration. After mixing for 24 hours, green bodies were formed by slip casting and bisque-firing at 1000°C for 2 h in air, in order to promote necking of the alumina particles. The samples were sintered at 1600°C for 2 h in air, while covered with high purity alumina power inside the furnace, resulting in dense samples (~99% relative density) without (detectable amounts of) carbon. In addition, undoped alumina green bodies were sintered in a graphite furnace at 1600°C for 6 h under flowing He and resulted in a final relative density of 97%.

For XRD measurements, samples were sectioned in order to measure from the bulk of the samples. For Raman spectroscopy measurements, samples were sectioned and polished using a diamond suspension on polishing cloths starting from a diamond size of 125 μm and concluding with a diamond size of 75 μm in order to obtain a flat surface. After polishing, the samples were ultrasonically cleaned in acetone, and then rinsed in ethanol and isopropanol. Before the measurements, the samples were plasma etched (Fischione plasma cleaner, model 1020), with a gas mixture of 25% oxygen and 75% argon at a power of 660 W for 10 min aiming to remove hydrocarbons from the sample's surface before the measurements.

For scanning electron microscopy (SEM) measurements of the microstructure, samples were sectioned, polished using a diamond suspension on polishing cloths starting from a diamond size of 30 μm and concluding with a diamond size of 1 μm, and thermally etched at 1200°C for 2 h under He.

For scanning / transmission electron microscopy (S/TEM), samples were sliced, trepanned to 3 mm diameter disks, mechanically ground to a thickness of ~100 μm, mechanically dimpled, and ion milled to perforation with Ar at 4–8 kV using a Gatan 695 Precision Ion Polishing System (PIPS-II).

For WDS measurements, the samples were also polished using a diamond suspension on polishing cloths, starting from a diamond size of 30 μm and concluding with a diamond size of 1 μm. After polishing, the samples were ultrasonically cleaned in acetone, and then rinsed in ethanol and isopropanol. In order to prevent charging during the WDS measurements (under the electron beam), the samples were coated with a 10 nm thick coating of Au. The samples were coated with Au by sputtering (ATC2200 Sputtering System, AJA International) using a 99.99% pure gold target at a power of 25 W for 150 s, in 99.99% Ar. A 99.99% oxygen plasma etching system was used at a power of 200 W for 15 min to clean the samples' surfaces in-situ before sputtering to remove hydrocarbons from the surface before Au coating.

#### 3.1.1.2 Carbon Doped Alumina

Using the same methodology, samples were prepared using the same high purity (99.99%) α-$Al_2O_3$ powder mentioned above. Doping with carbon was done by infiltrating bisque-fired (1000°C for 2 h) green bodies with glucose solutions. During the infiltration process, the fired green bodies were placed in a beaker inside a vacuum desiccator for 2 h, and then different water-based glucose solutions (Sigma-Aldrich, G5767, St. Louis, Missouri), as summarized in section 3.1.1.1, were added to the beaker (inside the vacuum desiccator, without breaking vacuum). Samples were held in the vacuum desiccator for ~24 h to ensure infiltration. After 24 h the beakers were removed from the vacuum desiccator and heated to ~60°C in order to reduce the contact angle of the glucose solution on alumina and further promote infiltration. The glucose-water solution was removed from the beakers and the samples were dried first at room temperature for ~12 hours and then at 110°C in air furnace for 5 h. Once dried, the samples were pyrolyzed (to convert the sugar to carbon) in flowing Ar gas at 600°C for 2 h. The infiltration and pyrolysis processes resulted in different wt.% of carbon in the samples, depending on the amount of glucose in the water solution and the number of infiltration and pyrolysis steps, as described before. Infiltrated alumina samples were then sintered at 1600°C for 6 h (heating rate 15°C/min) in a high-temperature resistance furnace (Thermal Technology Inc, Model 1000) with graphite heating elements and crucibles under flowing He (99.995%). The samples were covered with high purity alumina power inside graphite crucibles. The

samples were furnace-cooled under flowing He at a maximum cooling rate of ~60°C/min. Other carbon doped alumina samples were thermally annealed at 1900°C for 6 h and then at 1600°C for 6 h, part of them after sintering at 1600°C for 6 h.

## 3.2 The Influence of Sintering Atmosphere on the High-Temperature Solubility Limit of Mg in Alumina

Using the same methodology described in section 3.1.1.1, samples were prepared using the same high purity (99.99%) α-$Al_2O_3$ powder mentioned above, to which a water solution containing 10 wt.% magnesium nitrate ($Mg(NO_3)_2 \cdot 6H_2O$, (Merck KGaA, Germany)) was added. Samples were then sintered at 1600°C for 2 h in air and then thermally annealed at 1600°C for 20 h in a high-temperature resistance furnace (Thermal Technology Inc, Model 1000) with graphite heating elements and crucibles under flowing He (99.995%) and furnace-cooled at a maximum cooling rate of ~60°C/min.

## 3.3 Characterization

### 3.3.1 Density

The density of samples ρ was determined using the Archimedes method following ASTM standard c 20-92:

$$\rho = \left( \frac{D}{W - S} \right) \cdot \frac{1}{\rho_{Al_2O_3}} \tag{18}$$

where $D$ is the dry weight, $W$ is the saturated weight, $S$ is the suspended weight and $\rho_{Al_2O_3}$ is the theoretical density of alumina which is 3.98 gr/cm$^3$.

### 3.3.2 X-Ray Diffraction

X-ray diffraction (XRD) was used to identify phases. XRD patterns were acquired using a X-ray powder diffractometer (Rigaku Smart Lab X-ray Diffractometer, Tokyo, Japan) with a Cu Kα rotating anode, operated at 200mA and 45 kV, with 0.3 mm receiving slits. Diffraction patterns were acquired at steps of 2θ = 0.01° and 1.2 s/step exposure.

### 3.3.3 Raman Spectroscopy

Raman spectroscopy was used to confirm the presence of secondary phases of carbon in the carbon doped alumina samples, indicating that the amount of carbon in the alumina grains was at the solubility limit (the graphite secondary phase was not detected by XRD, apparently because of the detection limit of graphite in alumina for XRD). Raman measurements were acquired using a micro-Raman WiTec Alpha300 R spectrometer from undoped and carbon-doped alumina samples, using an objective of 100X with a 532 nm laser at a power of 8-10 mW. All the spectra were recorded under identical conditions with an integration time of 1 s, and 40 acquisitions per measurement. Before the measurements the samples were polished, ultrasonically cleaned in acetone, and then rinsed in ethanol and isopropanol and plasma etched.

### 3.3.4 SEM and S/TEM

SEM and S/TEM were used to characterize the microstructure of the carbon doped alumina samples. SEM was conducted using a FEI Quanta 200 E-SEM (Eindhoven, Holland) and a Zeiss Ultra-Plus field emission gun SEM (Oberkochen, Germany). Energy dispersive spectroscopy (EDS; Link Isis, Oxford Instruments) was also used to confirm the presence of secondary phases in the SEM samples. S/TEM was conducted using a Tecnai T-20 G2 at 200 kV (FEI, Eindhoven, Holland) and a monochromated and double aberration-corrected S/TEM (FEI Themis-Z 80–300 keV S/TEM) operated at 300 kV. Structural and chemical analysis of the interface region between the alumina grains and the neighboring carbon phase were conducted using STEM - EDS (EDAX, Tilburg, Holland) and electron energy loss spectroscopy (dual EELS: Gatan Quantum ER965, Pleasanton, CA).

### 3.3.5 WDS

The carbon concentration was measured using WDS (Oxford Instruments, High Wyecombe, U.K.) mounted on a SEM (FEI Quanta 200). A SEM accelerating voltage of 10 kV and a constant electron beam current of ~110 nA were used for WDS experiments. The measurements were acquired at a working distance of 11 mm, in spot mode, with a measurement time of 20 s. A LSM80N crystal was used as a monochromator for the WDS measurements. Non-coated pure graphite was used as a standard for carbon quantification. The carbon-K$\alpha$ peak was measured at a spectral position showing a maximum intensity. The background intensity was measured at two different spectral positions around the peak position. The background intensity at the peak position was calculated using linear interpolation.

Since thermal etching was not conducted, it was not possible to identify grain boundaries by SEM, making it problematic to differentiate between alumina grains, grain boundaries, and secondary phases of carbon. To overcome this difficulty, more than 500 WDS measurements were acquired from the carbon-doped alumina samples, at random locations across the cross-section of each sample, and data analysis was conducted following the method developed by Miller et al. [14]. The carbon concentration distribution frequency can be categorized into two main regions of volume interaction of the electron beam with the sample: 1) A region of interaction solely within the alumina grains (which is by definition the solubility limit for the two-phase equilibrated samples), and 2) a volume of interaction which overlaps with alumina grains and secondary carbon particles.

However, carbon concentration measurements are complicated, since the contribution of carbon contamination from electron beam interaction with the surface of the sample has to be taken into account. The carbon signal contributed from cracking adsorbed hydrocarbons can be measured by characterizing a sample that does not contain carbon in solution, and this value can be removed as a background signal from data acquired from carbon doped samples. The reference sample used in this study was undoped polycrystalline alumina which was prepared following the details given above. In addition, a (0001) oriented sapphire ($\alpha$-$Al_2O_3$) sample (99.99% purity provided by Gavish Industrial Technologies & Materials, Omar, Israel) was also used to compare the background carbon level with that of undoped alumina. To reduce the amount of carbon contamination as much as possible, the samples, the graphite standard, and the SEM sample holder were plasma etched in air (21% oxygen) at a base pressure of ~1.3 Pa for 20 min outside the microscope, at a power of 10 W. The chamber of the microscope was also plasma etched using the same conditions, and oil-free vacuum pumps were used during the measurements. In addition, the background signal of carbon due to hydrocarbon adsorption was quantified for each specific day of measurement since this value can change daily for a multi-user facility. 300 measurements were acquired from the undoped alumina and sapphire samples for analysis of the hydrocarbon contamination.

For the carbon content measurements, a ZAF correction factor was calculated using XPHI Software [43].

# 4. Results

## 4.1 The Influence of Carbon on Densification of Alumina

Table 1 summarizes the amount of glucose which was added during infiltration, subsequent sintering conditions, carbon concentration (above or below the solubility limit as measured by Raman spectroscopy) and the relative density of the sintered samples.

Table 1: The influence of carbon on densification of alumina.

| System | Amount of glucose in 100 mL of distilled water used in infiltration process [g] | Sintering conditions | Carbon concentration [above/below solubility limit] | Relative density [%] |
|---|---|---|---|---|
| Undoped alumina | - | 1600°C/ 6 h in air, heating/ cooling rates of 10°C/min | - | 99 |
| Gray alumina | - | 1600°C/ 6 h in a graphite furnace under flowing He, heating rate of 15°C/ min and cooling rate of 60°C/min | Below | 97.7 |
| Fully saturated carbon doped alumina | >47 | | Above | 80.5 |
| 2% carbon doped alumina | ~1 | 1600°C/ 6 h in a graphite furnace under flowing He, heating rate of 15°C/ min and cooling rate of 60°C/ min | Above | 87 |

| | | | | |
|---|---|---|---|---|
| 2% carbon doped alumina | ~1 | (1) 1600°C/6 h<br>(2) 1900° C/6 h<br>(3) 1600°C/6 h<br>In a graphite furnace, under flowing He heating rates of 15-25°C/ min and cooling rate of 60°C/ min | Above | 99.4 |
| 0.2% carbon doped alumina | ~0.27 | (1) 1900° C/ 6 h<br>(2) 1600°C/ 6 h<br>In a graphite furnace, under flowing He heating rate of 25°C/ min and cooling rate of 60°C/ min | Below | 95.7 |
| 0.1% carbon doped alumina | ~0.12 | 1600°C/ 2 h in a graphite furnace under flowing He, heating rate of 15°C/ min and cooling rate of 60°C/ min | Below | 94.9 |
| 0.4% carbon doped alumina | ~0.52 | | Above | 78.5 |

| | | | | |
|---|---|---|---|---|
| 0.9% carbon doped alumina | ~0.67 | | Above | 71.7 |
| 1.2% carbon doped alumina | ~1.6 | | - | 71.5 |
| 1.5% carbon doped alumina | ~2 | | - | 70.9 |
| 1.8% carbon doped alumina | ~2.4 | | - | 68.8 |
| 3% carbon doped alumina | | | - | 73.8 |

According to the density measurements, the relative density of the alumina decreases with increasing carbon content. This observation leads to the conclusion that the presence of a secondary carbon phase hinders densification of alumina. Figure 8 (a) presents a secondary electron (SE) SEM micrograph of the thermally etched surface from the cross-section of a 'fully saturated carbon doped alumina' sample, which found to reach only 80% of the theoretical density of alumina despite a 6 h sintering process at 1600°C, as shown in Table 1. In addition, a bimodal alumina grain size distribution is evident.

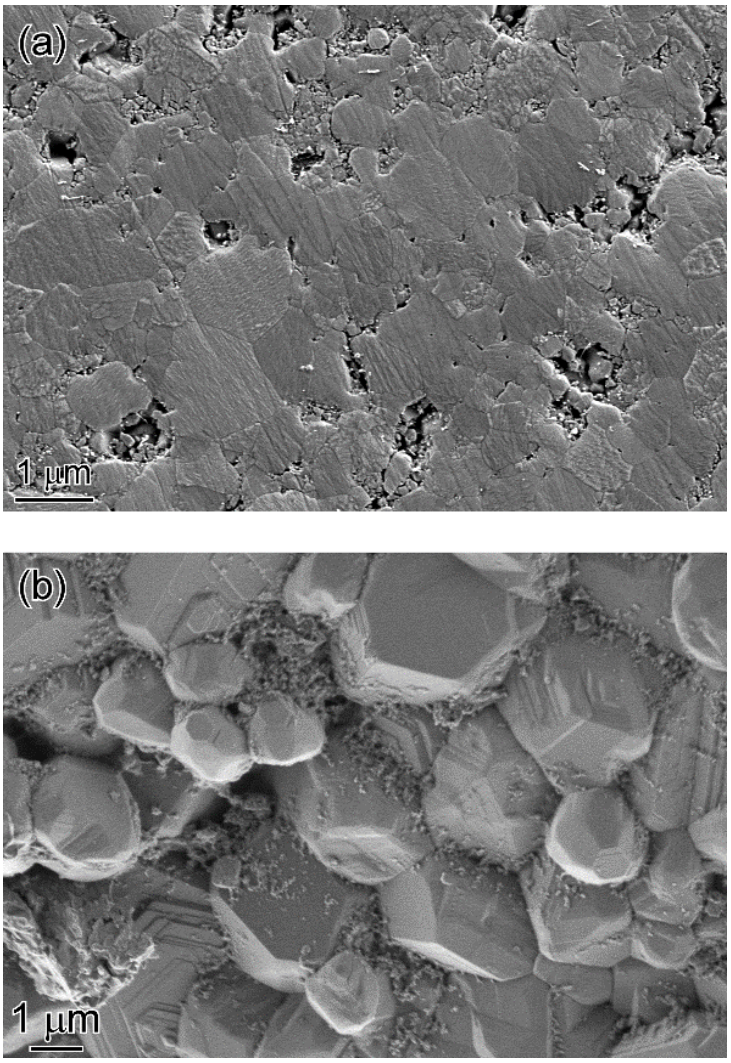


Figure 8: Secondary electron SEM micrographs showing the microstructure of sintered carbon doped alumina: (a) thermally etched surface from the cross-section of a sintered sample, and (b) a fracture surface.

Figure 9 presents secondary electron (SE) and backscattered electron (BSE) SEM micrographs of fracture surfaces from the '2% carbon doped alumina' samples, where Figure 9 (a) and (b) are from the samples which were sintered at 1600°C for 6 h, and Figure 9 (c) and (d) are from the same sample, after a heat treatment at 1900°C for 6 hours and another 6 h at 1600°C. It can be seen that the increased sintering time and temperature results in an increased alumina grain size and ripening of the carbon secondary phase.

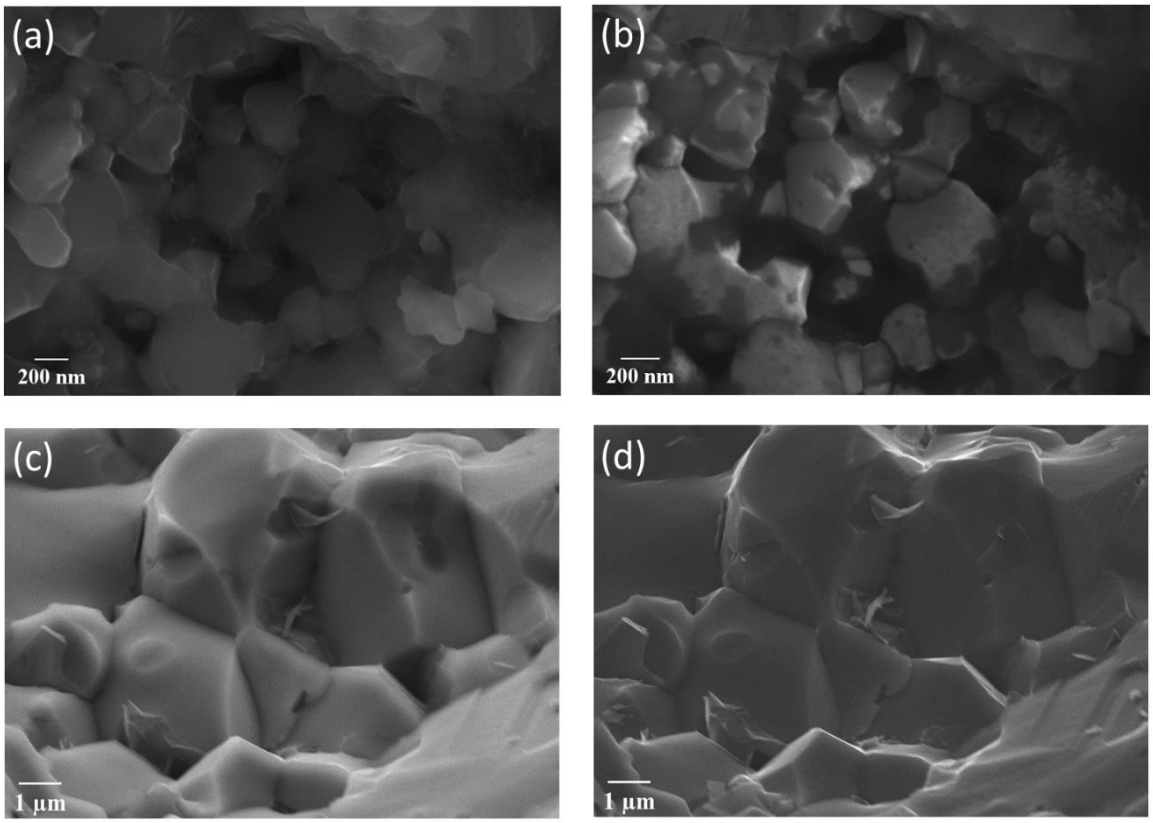


Figure 9: (a) SE and (b) BSE SEM micrographs of the fracture surface of carbon doped alumina which was doped by infiltration in a 2% glucose solution, which was sintered at 1600°C for 6 hours. (c) and (d) are SE and BSE SEM micrographs of the fracture surface of the same sample, after heat treatment at 1900°C for 6 hours followed by 6 hours at 1600°C, in a graphite furnace under flowing He.

## 4.2 The Solubility Limit of Carbon in Alumina

### 4.2.1 Confirmation of Carbon Saturated Alumina

The carbon content of the equilibrated alumina grains represents the solubility limit only if they are saturated with carbon, which can be experimentally confirmed if a secondary phase containing carbon exists after equilibration. The goal of this section is to confirm the existence of a carbon secondary phase, thus validating the WDS data presented in the next section.

XRD data for carbon saturated alumina sample that was furnace cooled from 1600°C is presented in Figure 10. The XRD pattern contains only alumina reflections, and additional peaks at ~32, 34, 38 and 42° which are not related to any carbon or C-Al-O phases (probably below the detection limit of the used XRD system) even though the sample was doped by two infiltration processes with a fully saturated glucose water solution. The assumption was that the carbon content of the carbon doped alumina was below the detection limit of XRD

(assuming crystalline graphite), and as a result Raman spectroscopy was used to confirm the presence of a second phase.

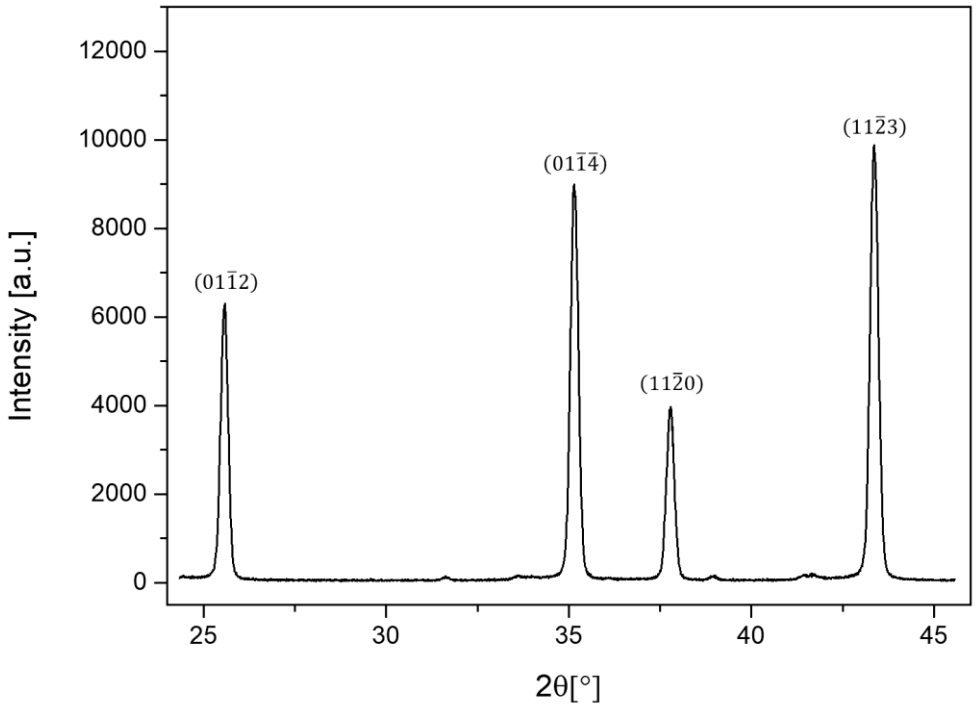


Figure 10: XRD pattern of carbon doped alumina sample, presenting only alumina reflections. Reflections from graphite (or any other phase) were not detected.

Figure 11 presents representative Raman spectra acquired from an undoped alumina sample (blue spectrum) and two carbon doped alumina samples (red and black spectra), with different carbon amounts. The spectrum obtained from undoped alumina includes peaks at 381, 418, 480 and 644 $cm^{-1}$, which are characteristic peaks of alumina [48]. The black spectrum obtained from a carbon doped alumina sample contains two characteristic peaks of $sp^2$-carbon, D and G at 1360 and 1583 $cm^{-1}$, respectively. The D peak corresponds to the breathing modes of $sp^2$ carbon atoms in rings and arises due to the symmetry breaking at the edges, and is therefore related to the disordered structure of graphite, and the G peak corresponds to the in-plane bond stretching of all pairs of carbon $sp^2$ atoms both in the rings and the chains [49,50,51]. Additional peaks are the 2D peak of graphite at 2696 $cm^{-1}$ and second-order peaks at 2450, 2957 and 3248 $cm^{-1}$, indicating the presence of crystalline graphite [52]. The red spectrum acquired from a carbon doped alumina sample infiltrated with less carbon than the sample indicated by the black spectrum, does not contain any characteristic peaks of carbon asserting the absence of any kind

of carbon or carbonaceous material, indicating a carbon content below the detection limit of Raman.

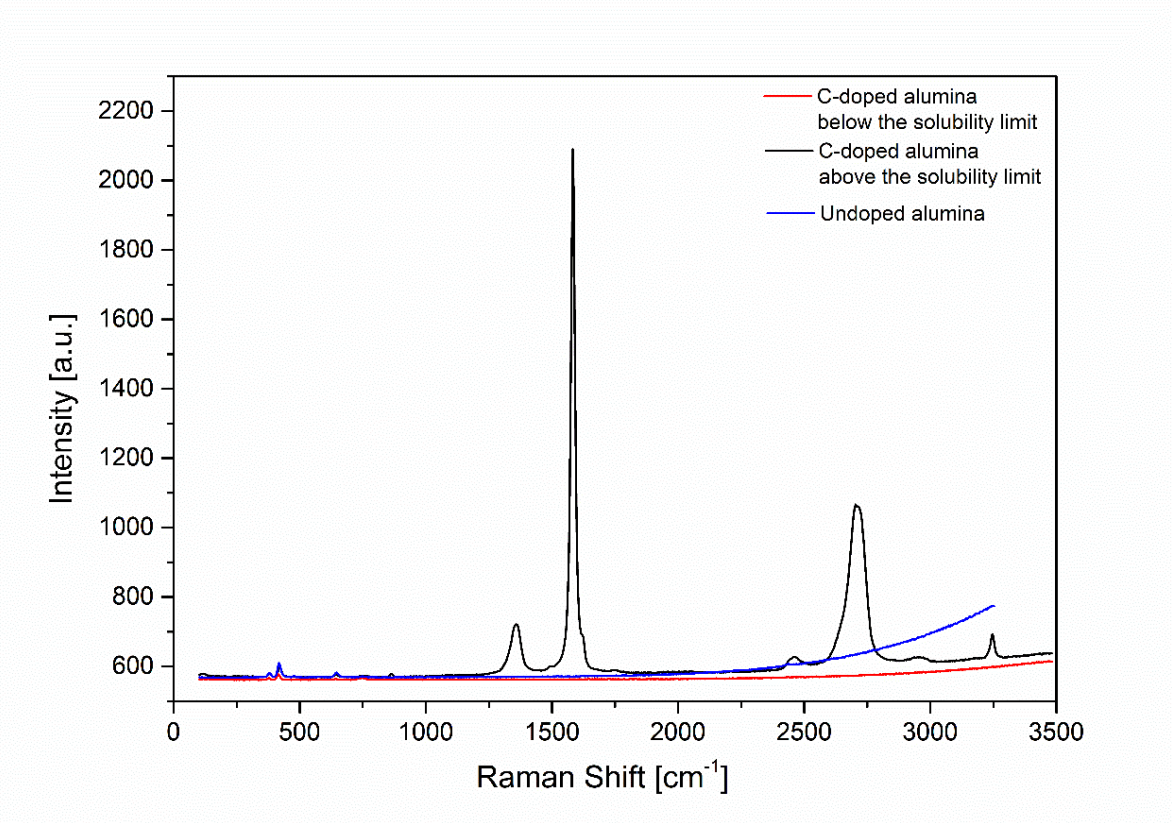


Figure 11: Representative Raman spectra acquired at a laser wavelength of λ=532 nm from undoped sintered alumina (blue line), and two carbon doped alumina samples (red and black lines). The characteristic carbon peaks D, G, 2D and second order peaks present in the black spectrum indicate the presence of graphite and a carbon content above the solubility limit of carbon in alumina. The absence of carbon characteristic peaks in the red and blue spectra indicates a carbon content below the detection limit of Raman.

### 4.2.2 Microstructure and Secondary Carbon Phase Characterization

For a detailed structural analysis of the secondary carbon phase, TEM and selected area electron diffraction (SAD) was performed. Figure 12 (a) presents a bright field TEM micrograph of the sintered carbon doped alumina showing secondary phase particles in between the alumina grains and at triple junctions. The SAD pattern presented in Figure 12 (b) was acquired from a similar region. Some reflections from graphite are visible in the SAD pattern, but the signal was not strong enough to confirm the presence of graphite.

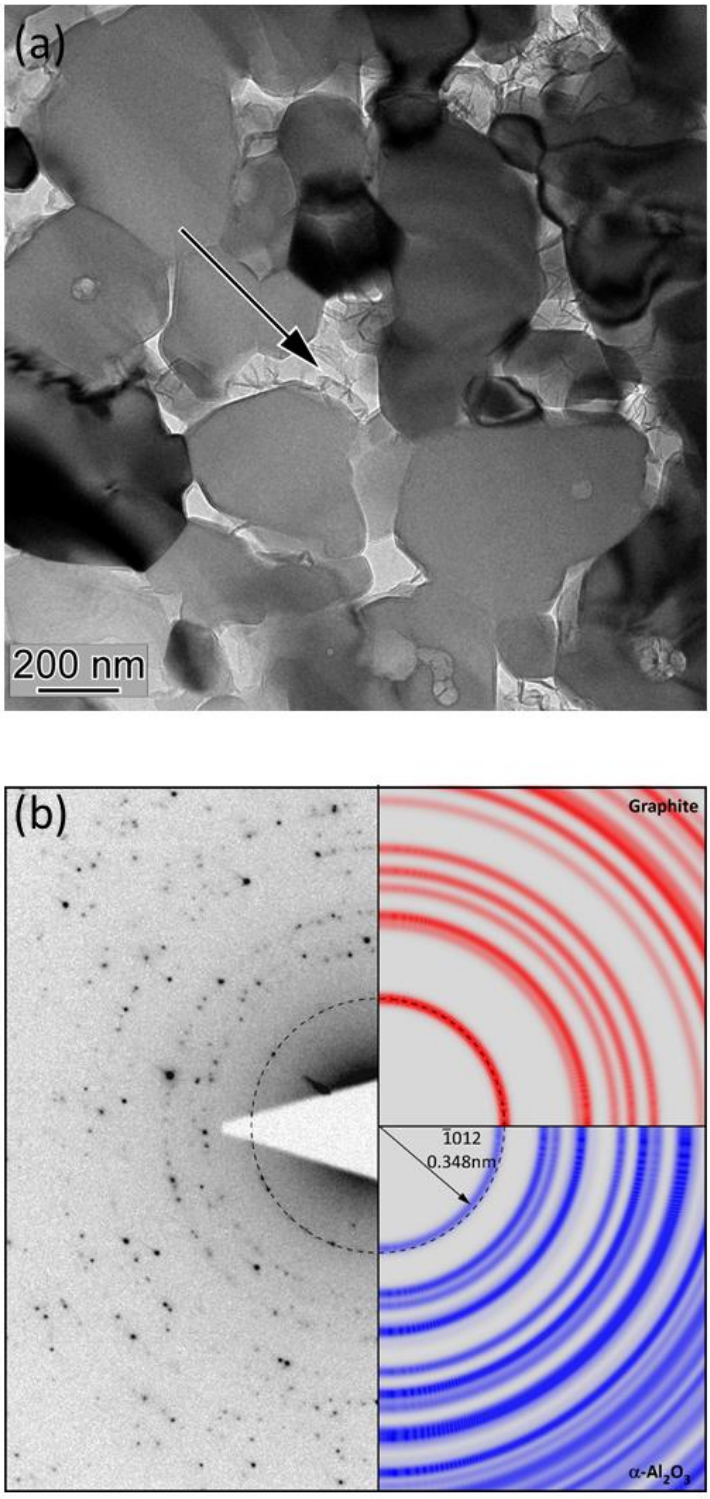


Figure 12: A bright field TEM micrograph of the 'fully saturated carbon doped alumina' samples (80% relative density). The arrow indicates a secondary phase at the triple junctions. (b) SAD pattern acquired from carbon doped alumina sample. The upper and lower right are simulated electron ring patterns of graphite (red) and alumina (blue).

Figure 13 presents STEM-EDS elemental mapping from a representative region arrowed in Figure 12 (a). Figure 13 (b) clearly shows that the secondary phase is carbon.

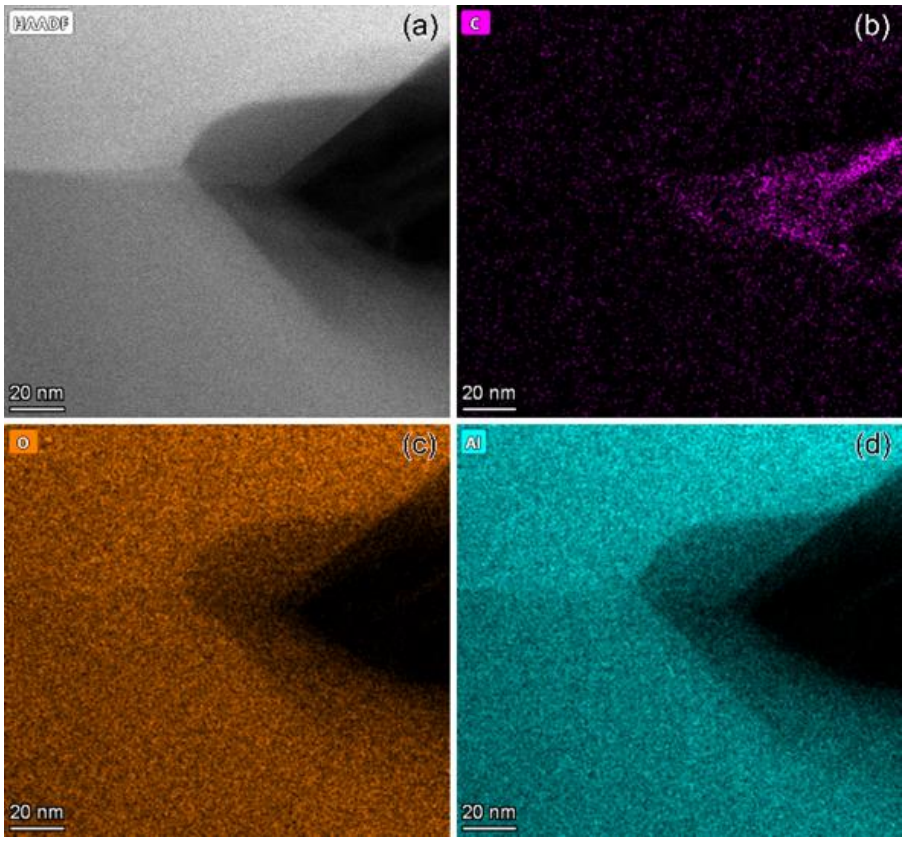


Figure 13: STEM-EDS elemental mapping (net intensity) from a representative region of a carbon-doped alumina sample containing both alumina and the secondary phase particle. (a) HAADF-STEM micrograph and (b)-(d) EDS elemental maps of carbon, oxygen and Al.

Additional inspection of the secondary phase by high angle annular dark field (HAADF) STEM (Figure 14) and EELS (Figure 15) confirm the secondary phase to be graphite. In Figure 14 a HAADF STEM micrograph of an edge on interface between an alumina grain and a graphite particle is shown. The {0002} planes of graphite and $(11\bar{2}0)$ and $(\bar{1}2\bar{1}6)$ planes of alumina are indicated. A low magnification annular dark field (ADF) STEM micrograph of the specimen is presented in Figure 15 (a), indicating the region from which an EELS measurement was performed (marked as +). Figure 15 (b) compares the experimentally obtained core-loss carbon-K$\alpha$ edge from the carbon-doped alumina sample (black spectrum) with that of a reference graphite (blue spectrum) and amorphous carbon (red spectrum) obtained from EELS data base [53,54]. The experimental EELS spectrum from the carbon phase is similar to that of graphite, corroborating the Raman and electron diffraction measurements obtained from the same carbon doped alumina specimen. Notably, the $\pi^*$ peak in the experimental spectrum does not rise sharply, in contrast to the reference graphite spectrum, resulting in a peak shift of 1.3 eV. The shift may be due to partial amorphization of the graphite by electron irradiation during the measurements at 300 kV.

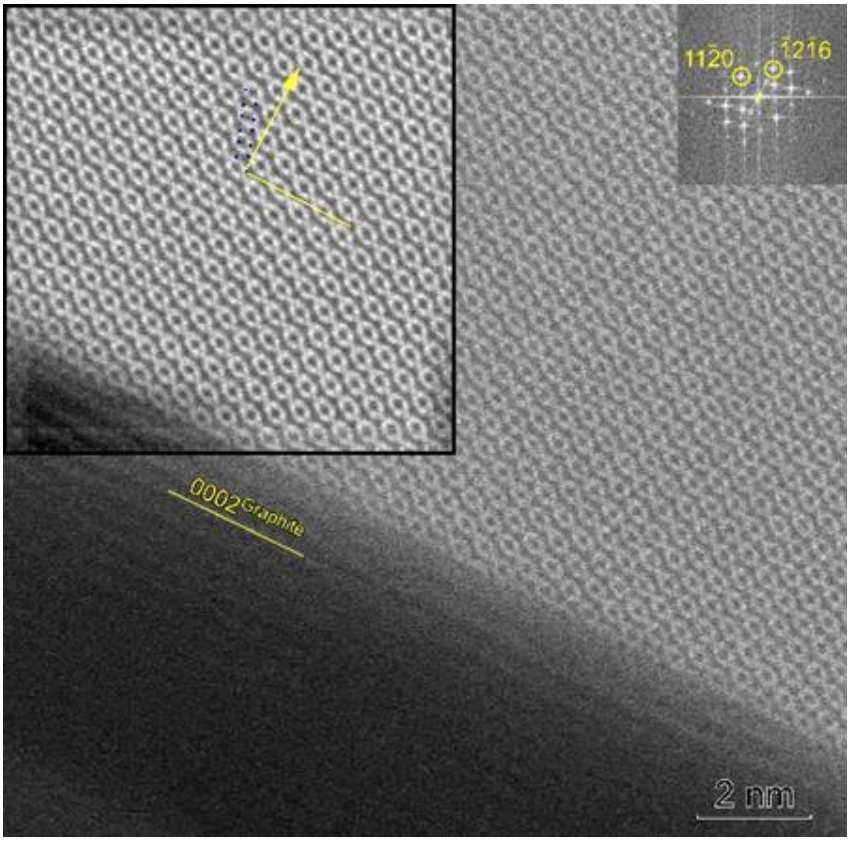


Figure 14: A HAADF-STEM micrograph of an edge-on interface between an alumina grain and a graphite particle. The area delimited with a black square was Bragg-filtered. The {0002} planes of graphite are indicated. The inset shows the FFT from the alumina grain in which $(11\bar{2}0)$ and $(\bar{1}2\,\bar{1}6)$ planes of alumina are indicated. The $(\bar{1}2\,\bar{1}6)$ plane is parallel to the interface with graphite, and is marked in the Bragg-filtered region of the STEM micrograph, and the positions of cations in the alumina are indicated by blue dots.

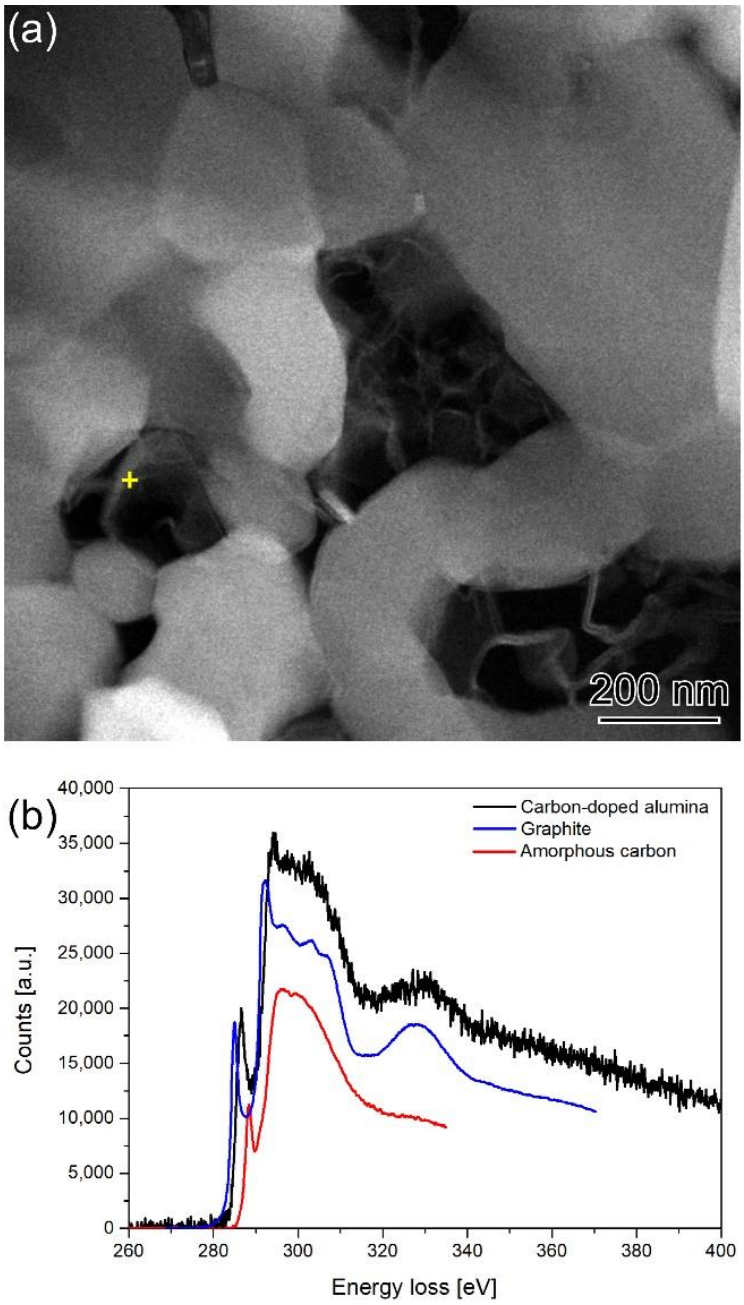


Figure 15: (a) ADF-STEM micrograph and (b) EELS spectra of the core-loss carbon-Kα edge from the carbon-doped alumina sample (black spectrum), compared with that of a reference graphite (blue spectrum) and amorphous carbon (red spectrum). The EELS spectra was acquired from the region indicated by a + in (a). The spectrum from graphite and amorphous carbon were reproduced with permission from [53,54].

### 4.2.3 WDS Measurements of Carbon Content

#### 4.2.3.1 Contamination

While the samples were demonstrated to be saturated with carbon, WDS measurements of the solute content must take into account deposition of carbon on the surface of the samples during WDS acquisition due to cracking of adsorbed hydrocarbons. To estimate the carbon contribution from the microscope (often called carbon contamination or ' Schmutz'), the carbon X-ray photon intensity (with a reference to a graphite standard) was measured as a function of electron dose (measurement time) and incident energy, taken from undoped alumina specimens. Figure 16 (a) presents a comparison between four different days of WDS measurements of carbon X-ray photon intensity ratio, as a function of measurement time. Interestingly, during each day of measurement the carbon signal from contamination saturates within 20 seconds of electron dose and remains relatively stable afterwards. In addition, the first measurement (after 20 seconds) is significantly different for each day. These results showed the consistency in the contamination amount on a specific day of measurement. Figure 16 (b) presents a comparison of three different measurement locations from the undoped alumina sample, on the same day of measurement. The intensity ratio (which correlates to the contamination amount) is relatively stable across the surface of the sample. Figure 16 (c) presents the measured contamination intensity ratio formed on sapphire compared with that from undoped sintered alumina, on the same measurement day, demonstrating similar contamination rates of sapphire and undoped alumina. Figure 16 (d) presents a SE SEM micrograph of the surface contamination typical from spot irradiation of an alumina sample.

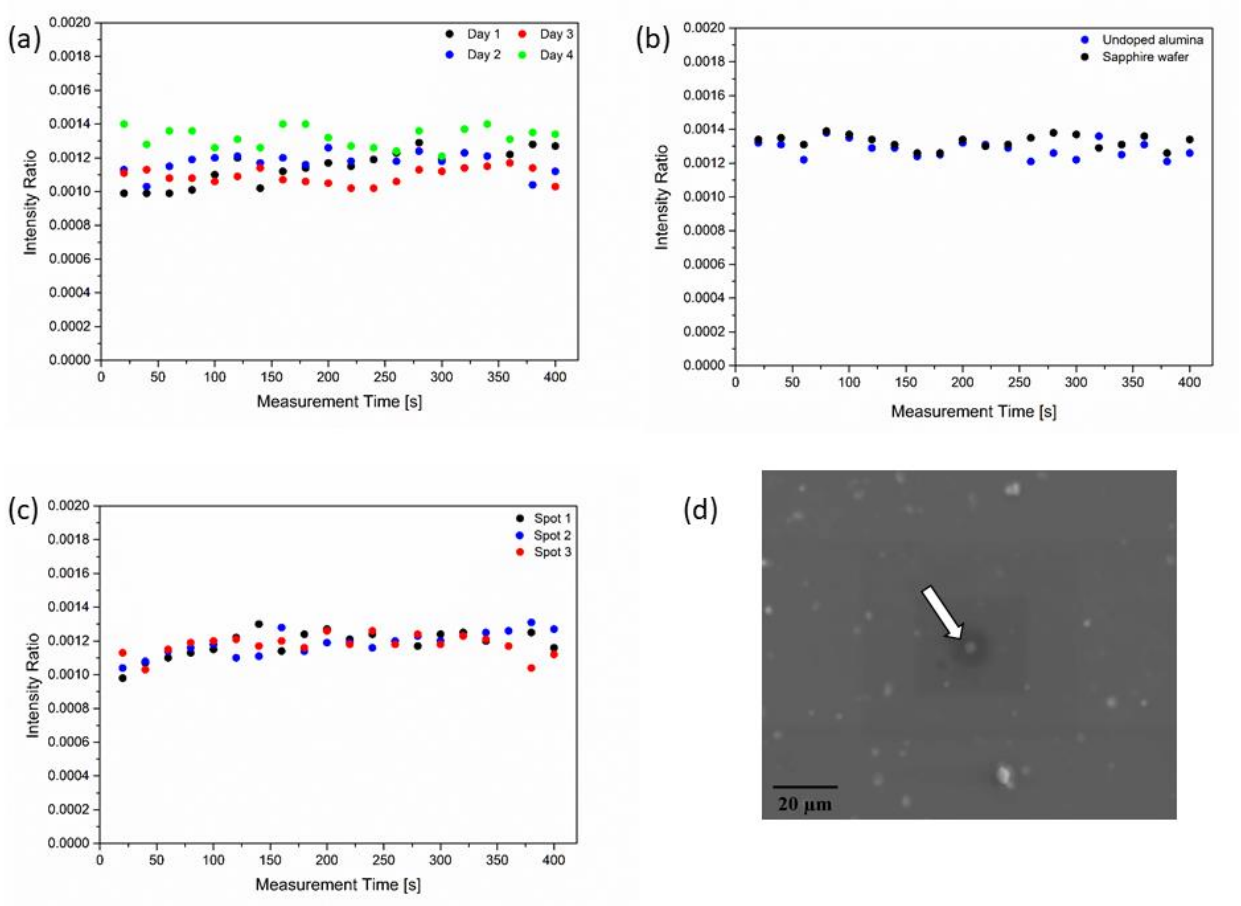


Figure 16: (a) WDS measurements of X-ray photons intensity ratio as a function of measurement time, acquired from sintered undoped alumina, Au coated samples, with compression between different days of measurements. (b) A comparison between the X-ray photon intensity ratio measured from sintered undoped alumina and sapphire samples (both Au coated) on the same day of measurements. (c) A comparison between the X-ray photon intensity ratio measured from different spots across a specific sintered undoped alumina sample, on the same measurement day. (d) A SE SEM micrograph of the contamination spot (arrowed). The rectangular contrast is from additional contamination resulting from imaging at a higher magnification (smaller scan-area) before this specific micrograph was acquired.

Figure 17 presents WDS measurements of the contamination intensity ratio, measured from the undoped alumina sample as a function of the incident SEM electron beam energy. The presented trend apprises the hydrocarbon-bond cracking potential depending on the incident beam energy and cross section. The intensity ratio decreases with increasing electron beam energy, due to a decreasing cross section and increasing penetration depth of the electron beam into the sample.

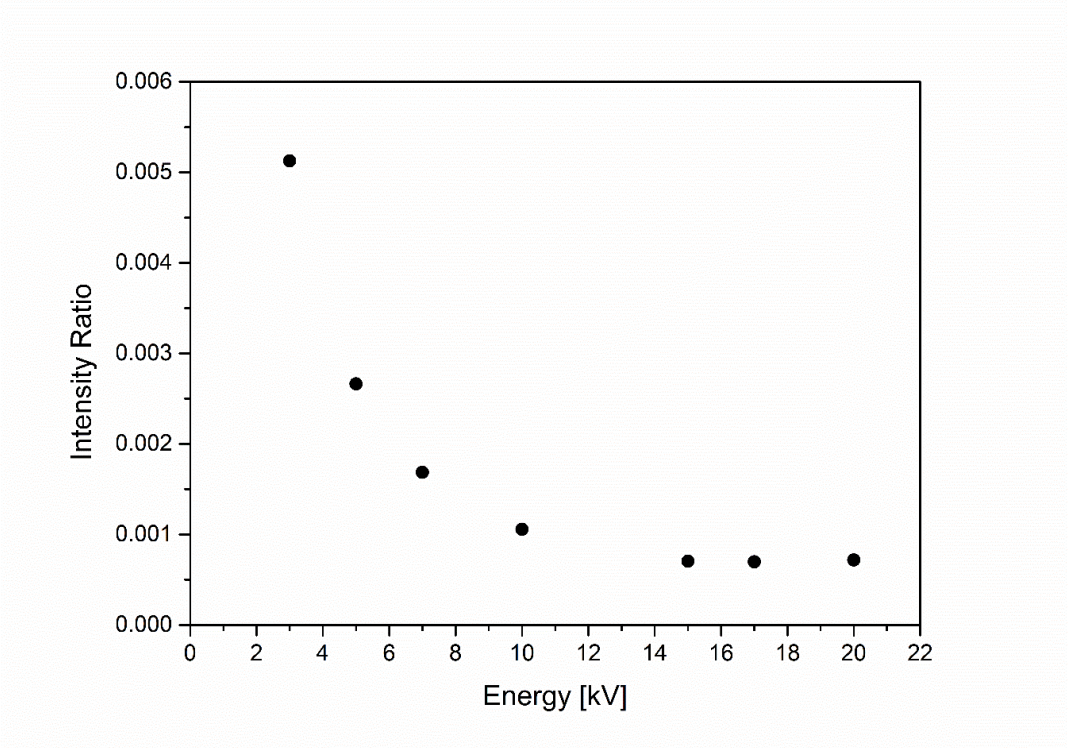


Figure 17: WDS measurements of carbon contamination, measured from an undoped alumina sample (presented as intensity ratio) as a function of the incident electron beam energy.

After measurements and removal of the carbon contamination intensity ratio, the carbon content measurements can be done (the background was always less than the carbon concentration in the carbon doped alumina samples).

#### 4.2.3.2 Solubility Limit Measurements

Figure 18 (a) presents the histogram of the carbon-Kα X-rays intensity ratio, after removal of the background contamination signal determined from the undoped alumina on the specific day of measurement and consideration of the Au coating. As explained in the experimental methods section, a WDS measurement histogram will consists of two regions, a low intensity ratio region, which correlates to the solute carbon content in the alumina grains, and the high intensity ratio which is related to the grain boundary excess and secondary phase(s). Figure 18 (b) presents the lower intensity ratio region (from 0.00002 to 0.0017), converted into carbon concentration after considering the ZAF correction factor. The concentration regime is fitted with a Gaussian curve (in red) to identify the peak position.

The peak at 3940 ± 906 ppm correlates to the solubility limit of carbon in alumina at 1600°C, with a detection limit of 15 ppm.

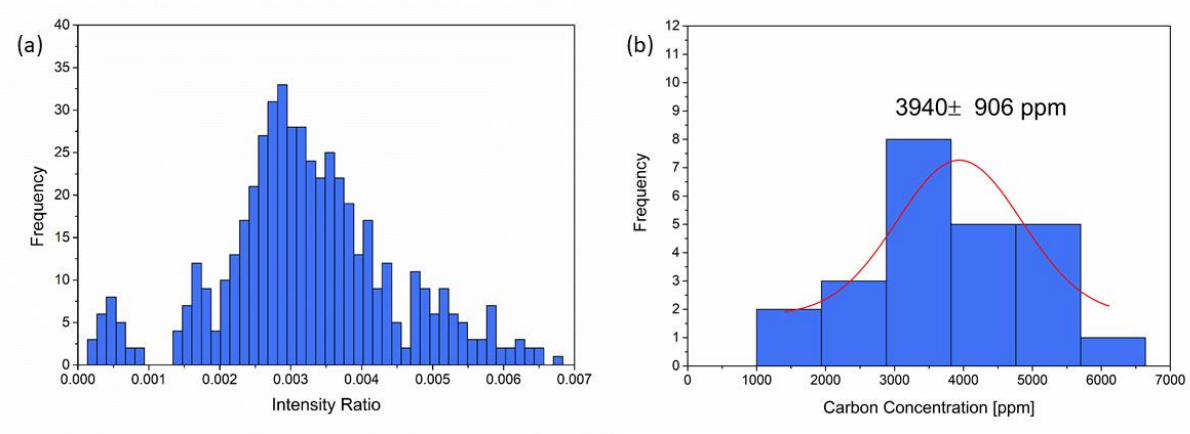


Figure 18: (a) Histogram of the X-ray photon intensity ratio measurements from carbon doped alumina samples rapidly cooled from 1600°C (after removal of the background contamination signal determined on the specific day of measurement and consideration of the Au coating). (b) presents a magnified section of the histogram focusing on the low-intensity ratio regime, which is correlated to X-ray photons emanating from a volume of interaction limited to only carbon saturated alumina (without a signal from the graphitic secondary phase) and converted to carbon concentration using the ZAF correction factor.

#### 4.2.3.3 WDS Measurements of One Phase System

In order to corroborate the carbon solubility limit value, the carbon content was measured from samples which were confirmed to contain carbon below the solubility limit. This included the "gray alumina" (undoped alumina sintered in a graphite furnace) and the "0.2% carbon doped alumina sample" (see Table 1).

Figure 19 presents representative Raman spectra acquired from undoped alumina sintered in air (black spectrum), “gray alumina” (undoped alumina sintered in a graphite furnace) (blue spectrum) and "0.2% carbon doped alumina" (red spectrum). No peaks characteristic of carbon was observed in any of the samples, which means the carbon content is below the solubility limit of carbon in alumina (or below the detection limit of Raman). Additionally, peaks at 1457 and 1520 $cm^{-1}$ were observed inconsistently in undoped and carbon doped alumina samples with carbon content below the solubility limit of carbon in alumina.

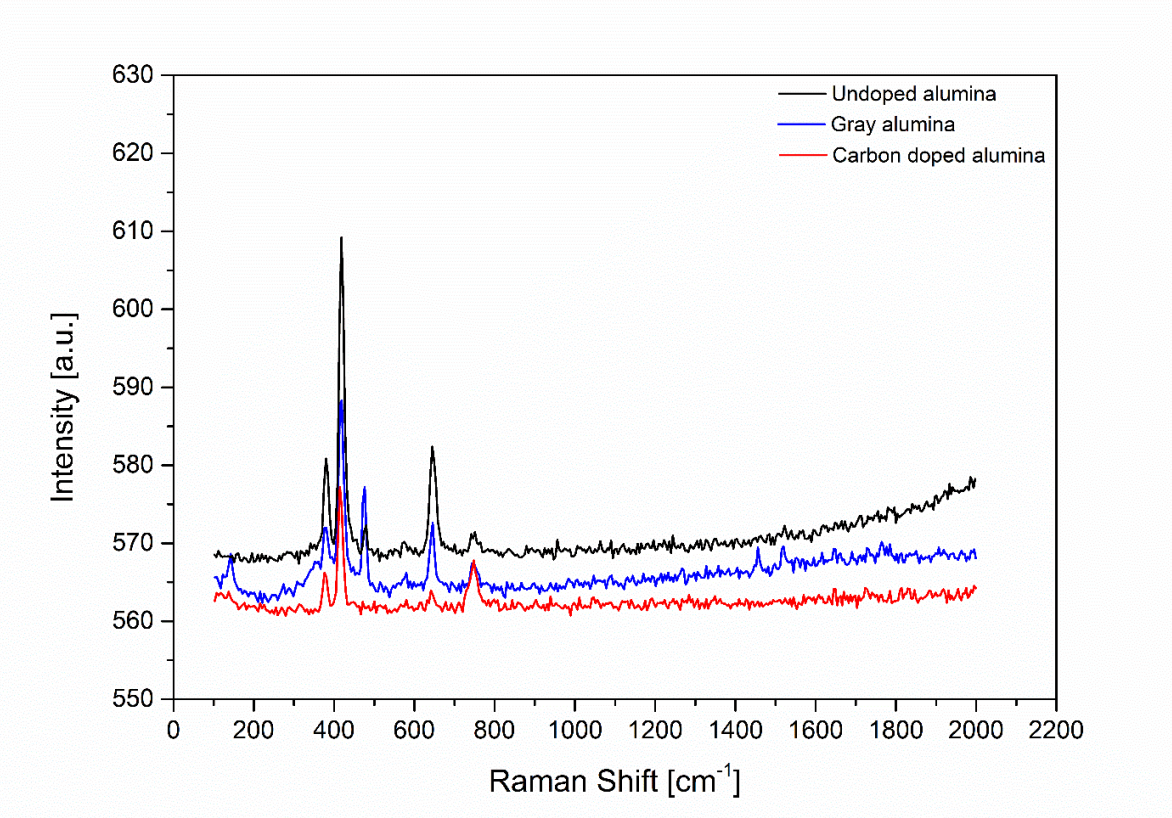


Figure 19: Representative Raman spectra acquired at a laser wavelength of λ=532 nm from undoped alumina sintered in air (black line), gray alumina, which is an undoped alumina sample sintered in a graphite furnace, under flowing He (blue line) and carbon doped alumina (red line). No observation of carbon characteristic peaks indicates a carbon content below the detection limit of Raman.

The WDS measurements resulted in ~1476 ppm and ~453 ppm of carbon in the "0.2% carbon doped alumina" and the "gray alumina", respectively, with a detection limit of ~22 ppm

## 4.3 The High-Temperature Solubility Limit of Mg in Alumina

### 4.3.1 Confirmation of Mg Saturated Alumina

Figure 20 presents an XRD pattern acquired from a Mg-saturated alumina sample that was furnace-quenched from 1600°C. The reflections in the XRD data confirm the presence of $MgAl_2O_4$ (Mg spinel) in addition to alumina. The presence of the secondary phase necessarily means that the alumina grains are saturated (at the solubility limit) with Mg.

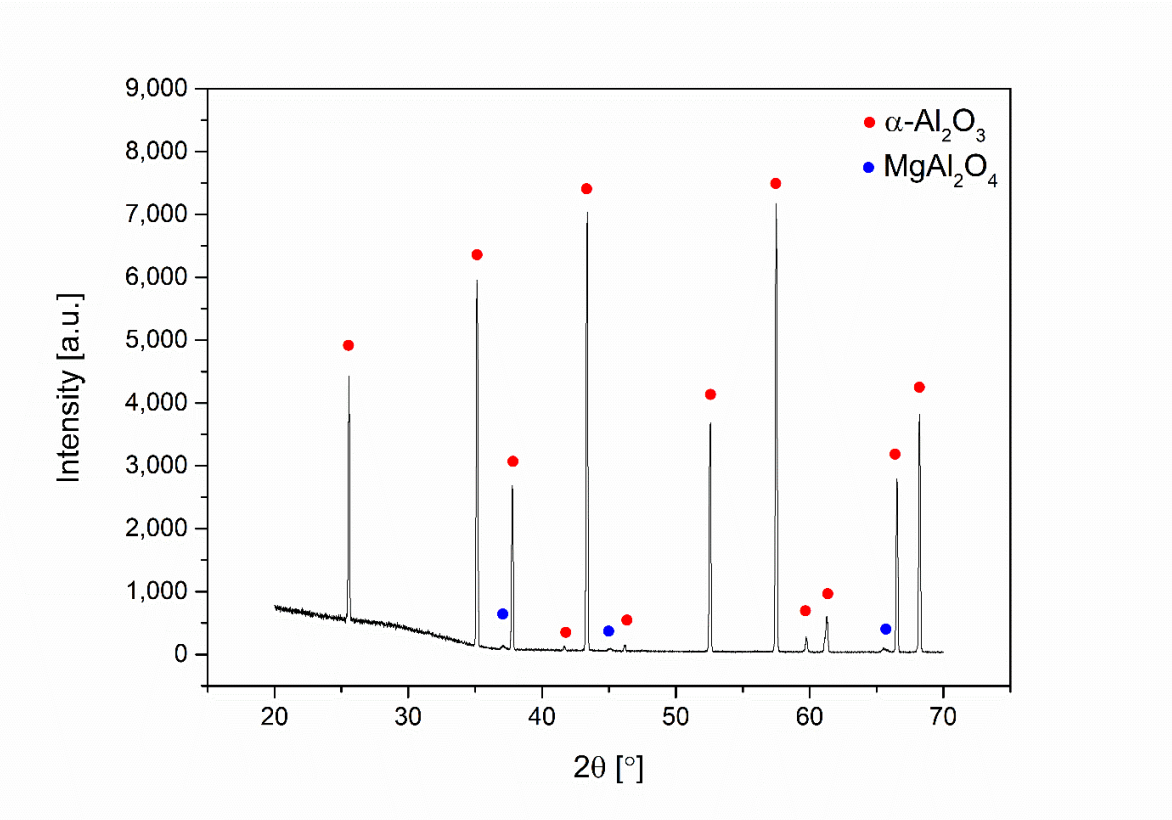


Figure 20: XRD pattern confirming the presence of alumina, and binary and ternary phases, thus ensuring saturation of the alumina grains with Mg.

Figure 21 presents a representative Raman spectrum acquired from undoped alumina samples sintered in air (black spectrum), and a Mg doped alumina sintered at a relatively low oxygen partial pressure, in a graphite furnace under flowing He (blue spectrum). The observed peaks at 379, 418, 578, 643 and 753 $cm^{-1}$, which are related to the alumina phase [48], are relatively close to the characteristic peaks of Mg spinel [55]. The changes in the intensities of the peaks and the peak expansion at 753 $cm^{-1}$ in the Mg doped alumina can be related to the presence of Mg spinel secondary phase (corroborating the XRD data). No peaks characteristic of carbon were observed in any of the samples, which means the carbon content is below the solubility limit of carbon in alumina (or below the detection limit of Raman).

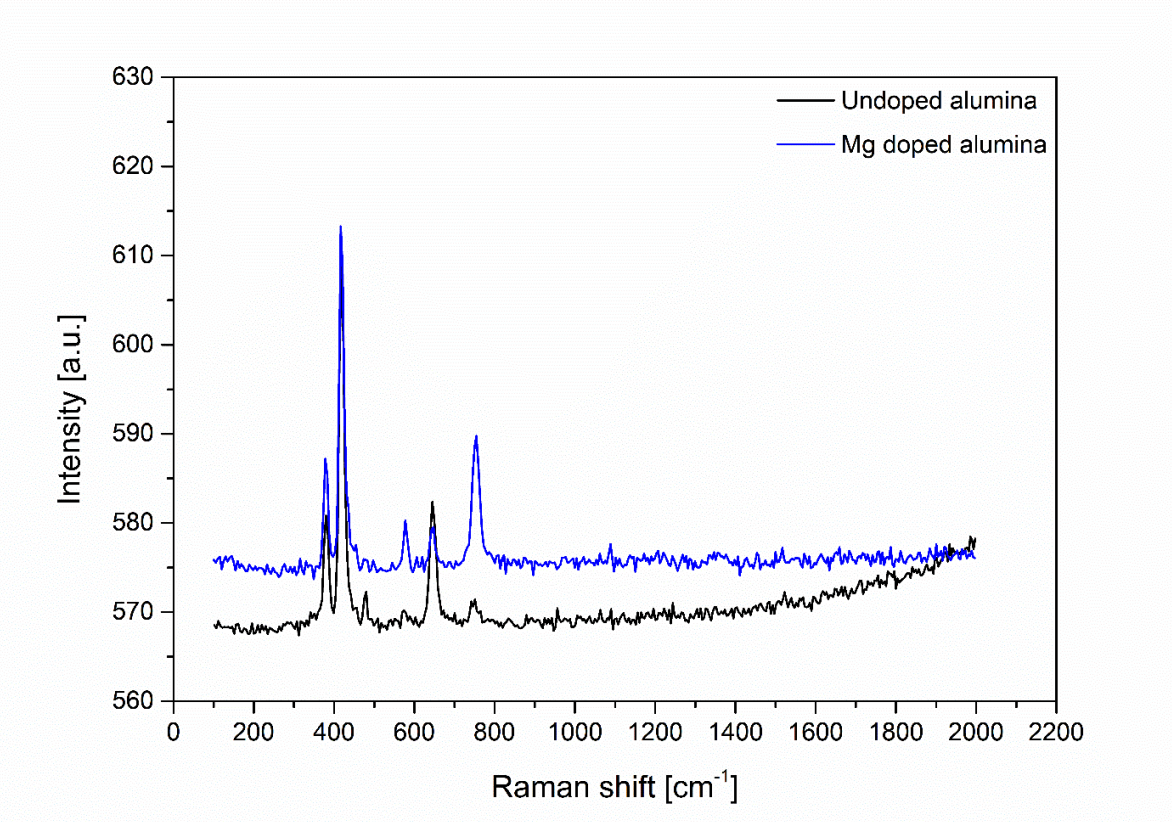


Figure 21: Representative Raman spectra acquired at a laser wavelength of λ=532 nm from undoped alumina (black line), and Mg doped alumina sample sintered in air and annealed at 1600C for 20 h at a relatively low oxygen partial pressure, in a graphite furnace, under flowing He (blue line). The absence of carbon characteristic peaks in the spectra indicates a carbon content below the detection limit of Raman.

Figure 22 presents a SE SEM micrograph of the fracture surface of a Mg-doped alumina sample.

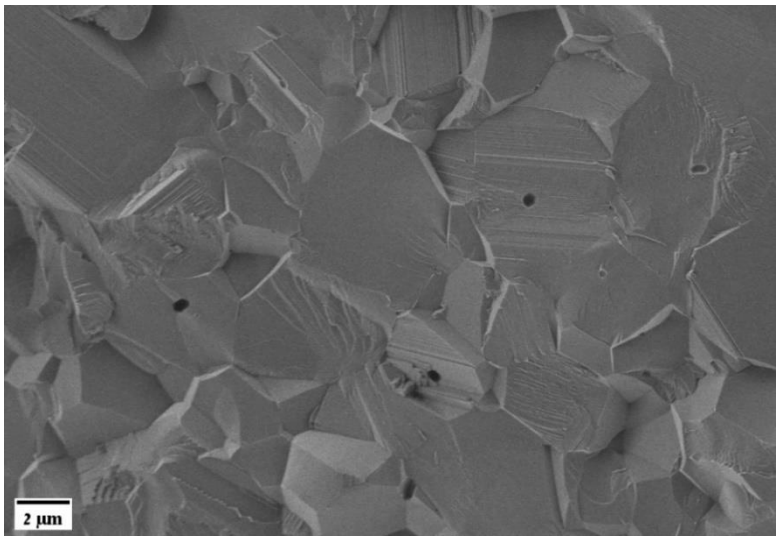


Figure 22: A SE SEM micrograph of the fracture surface of a Mg doped alumina sample sintered in air and annealed for 20 h at a relatively low oxygen partial pressure. The sample had a 95% relative density.

### 4.3.2 WDS Measurements of Mg Content

The amount of Mg in the samples was determined using WDS, from samples sintered at 1600°C for 2 h in air and then heat treated in a graphite furnace, under flowing He (which correlates to a relatively low oxygen partial pressure) for 20 h, and rapidly cooled from 1600°C inside the furnace. Figure 23 (a) presents the histogram of the Mg-Kα X-ray intensity ratio measurements, and Figure 23 (b) presents the lower intensity ratio region (from 0 to 0.012) after conversion to Mg concentration using the ZAF correction factor. The first peak at 166± 42 ppm correlates to the solubility limit of Mg in alumina at 1600°C, at a relatively low oxygen partial pressure (compared to air) with a detection limit of 3 ppm. The Gaussian curve indicated in red was fitted to the data to identify the peak position.

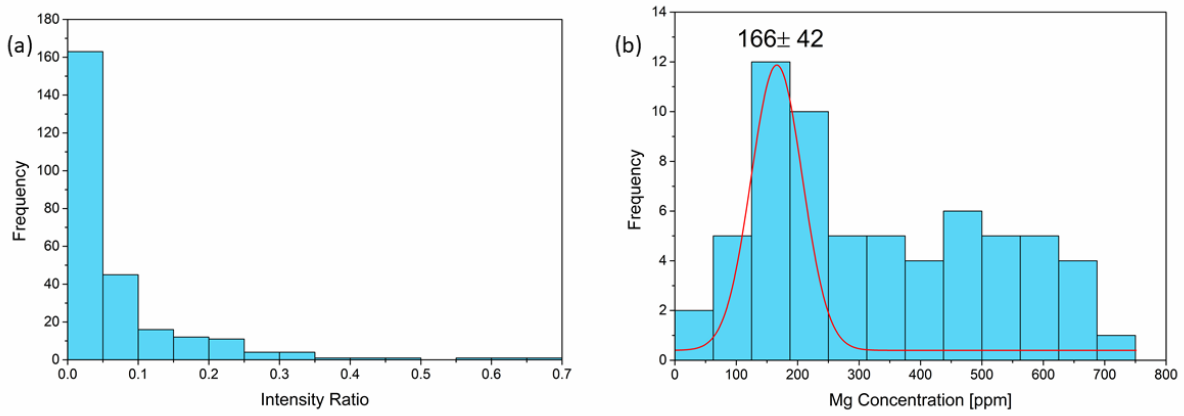


Figure 23: (a) Histogram of the Mg-Kα X-rays photon measurements from Mg doped alumina samples annealed at a relatively low oxygen partial pressure and rapidly cooled from 1600°C. (b) is a magnified section of the histogram focusing on the low intensity ratio regime, which is correlated to X-ray photons emanating from a volume of interaction limited to only Mg saturated alumina, without a signal from the Mg spinel secondary phase (the first peak) and from the overlap with grain boundaries (the second peak).

### 4.3.3 WDS Measurements of Carbon Content

As shown by Raman (Figure 23) the Mg doped alumina samples do not contain a carbon second phase. However, some carbon amount is assumed to dissolve in the samples during the long annealing in a graphite environment. A WDS measurement of the carbon content was done to determine the amount of dissolved carbon. The WDS resulted in ~1500 ppm of carbon in the Mg doped alumina, with a detection limit of ~53 ppm.

# 5. Discussion

## 5.1 The High-Temperature Solubility Limit of Carbon in Alumina

The solubility limit of carbon in alumina at 1600°C was found to be 3940 ± 906 ppm. Four possible point defects were taken into consideration to accommodate the dissolution of carbon in carbon doped alumina [38,41,56,57] which using Kröger–Vink notation are:

$$2CO \xrightarrow{Al_2O_3} 2C_{Al}{}' + 2O_o{}^x + V_O{}^{\bullet\bullet} \quad (19)$$

$$CO_2 \xrightarrow{Al_2O_3} C_{Al}{}^{\bullet} + V_{Al}{}''' + 2O_o{}^x + V_O{}^{\bullet\bullet} \quad (20)$$

$$Al_4C_3 \xrightarrow{2Al_2O_3} 3C_O{}'' + 4Al_{Al}{}^x + 3V_O{}^{\bullet\bullet} \quad (21)$$

$$3CO_2 \xrightarrow{Al_2O_3} 3C_i{}^{\bullet\bullet\bullet\bullet} + 4V_{Al}{}''' + 6O_o^x \quad (22)$$

Eq (19) describes $Al^{3+}$ substitution by $C^{2+}$ cations with charge compensation via the formation of oxygen vacancies. Eq. (20) describes $Al^{3+}$ substitution by $C^{4+}$ cations with charge compensation via the formation of oxygen and Al vacancies. Eq.(21) describes $O^{2-}$ substitution by $C^{4-}$ which will also be charge-compensated via the formation of oxygen vacancies. Eq. (22) describes $C^{4+}$ in the interstitial sites of the alumina crystal, charge compensated by oxygen and Al vacancies. Equations 19-21 have been discussed in the literature, where Eq. (21) would be the situation for a low oxygen partial pressure leading to the formation of carbon anions.

Akselrod et al. studied the defect chemistry of the alumina-carbon system prepared under strongly reducing conditions in the presence of graphite, using thermoluminescent dosimetry (TLD). They reported on $F^+$ center formation (one electron in the anion vacancy field), which required the presence of charge compensation in the lattice via $Al^{3+}$ substitution by $C^{2+}$ cations, as descried in Eq. (19) [36]. However, according to DFT calculations, at low oxygen partial pressures the preferred defect for dissolution of carbon in alumina is substitution of oxygen by carbon anions, which is charge compensated by oxygen vacancies, as described in Eq. (21) [40,41]. Similar to the carbon doped alumina system, carbon was found to substitute oxygen in carbon doped $TiO_2$ [58]. It can be assumed, according to the relatively small radius of $C^{4+}$,

that a small amount of carbon may exist in the interstitial sites, which is charge compensated by Al and oxygen vacancies [56]. Another possibility is that $CH_3^-$ will substitute oxygen anions in the structure, and be charge compensated by oxygen vacancies. It can be assumed $CH_3^-$ will form on the surface of alumina as reported in the literature, especially given the use of water in the infiltration process [59,60].

The strain energy associated with a single solute atom ($\delta\varepsilon$) can be estimated following Zener [61]:

$$\delta\varepsilon = 8\pi\mu r(\delta r)^2 \tag{23}$$

where $\mu$ is the shear modulus of the host lattice (alumina) which is ~$1.47\cdot10^{11}$ N/ $m^2$ [62], $r$ is the ionic radius of the solvent atom and $\delta r$ is the difference between the radius of the solvent and solute. For $Al^{3+}$ (0.054 nm ionic radius) substitution by $C^{4+}$ (0.016 ionic radius, assuming the carbon is going to the octahedral site and replacing the Al) [63] and ignoring the strain energy associated with the compensating defect, leads to a strain energy of $2.88\cdot10^{-19}$ J per solute atom. $O^{2-}$ (0.142 nm ionic radius) substitution by $C^{4-}$ (0.26 nm ionic radius) [62] would result in a strain energy of $7.3\cdot10^{-18}$ J per solute atom (ignoring the strain energy associated with the compensating defect and the change in formation energy of oxygen vacancy with change in partial pressure of oxygen). This simple estimate of the strain energy indicates a preference for Al substitution by carbon, but ignores the compensating defect, its strain energy, and possible interaction between the solute atom and the defect.

The measured solubility limit value of carbon in alumina at 1600°C is relatively large compared to Si (188 ppm), Mg (132 ppm) and Ca (51 ppm) which were equilibrated at a relatively high partial pressure of oxygen (in air) [14,19,24]. According to Futazuka et al., the solubility limit of Mg and Ca should not be significantly affected by the oxygen partial pressure, whereas the oxygen partial pressure should influence the solubility limit of carbon, due to the tendency to produce $CO/CO_2$ [41]. Zhu et al. calculated the defect formation energy in the carbon-alumina system at a relatively high oxygen partial pressure which resulted in $Al^{3+}$ substitution by $C^{2+}$ cations (Eq. (19)) [40].

The DFT simulations resulted in ~$4 \cdot 10^{-5}$ ppm solubility limit of carbon in alumina at ~1600°C [41] which is significantly lower than the experimental solubility limit measured by WDS in the present study. The difference between this calculated value and the measured carbon solubility limit may be due to the usual challenge of projecting absolute zero DFT simulations to high temperature and to finite gas partial pressures. A significant difference was also seen between the solubility limit of Ca in alumina predicted by DFT compared to measured values [19,20,41].

From knowledge of the secondary carbon (graphite) phase formation in our sintered carbon doped alumina samples, confirmed to be graphite from Raman spectroscopy and TEM-EELS (section 4.2.1), the oxygen partial pressure range during the sintering process can be estimated using the Gibbs–Helmholtz equation for the reaction [64]:

$$\frac{\partial\left(\frac{\Delta G^{\circ}}{T}\right)}{\partial T} = -\frac{\Delta H_T^{\circ}}{T^2} = -\frac{\Delta H_0}{T^2} - \frac{\Delta a}{T} + \frac{\Delta b}{2} - \frac{\Delta c}{T^3} \tag{24}$$

where $\Delta G^{\circ}$ is the change in Gibbs free energy at standard state, $\Delta H_T^{\circ}$ the standard reaction enthalpy at the temperature T, $\Delta H_0$ an integration constant which would be equal to the standard enthalpy of the reaction at 0 K only if the analytical expression for the change in heat capacity $\Delta C_p$ as a function of T was valid down to 0 K, and Δa, Δb and Δc are constants values for a specific element.

After integration:

$$\Delta G_T^{\circ} = \mathrm{I}T + \Delta H_0 - \Delta a T \ln(T) + \frac{\Delta b T^2}{2} - \frac{\Delta c}{2T} \tag{25}$$

where I is an integration constant and $\Delta G_T^{\circ}$ is the Gibbs free energy at T.

It is also known that

$$\Delta G_T^{\circ} = -RT \ln(K_P) \tag{26}$$

where $R$ is the gas constant and $K_P$ is the equilibrium constant of a certain reaction. For reaction

$$aA + bB \rightarrow cC + dD \tag{27}$$

the equilibrium constant will be

$$K_P = \frac{[D]^d [C]^c}{[B]^b [A]^a} \tag{28}$$

were $[X]^x$ is the concentration of element X with an exponent of its stoichiometric coefficient x.

In the case of a reaction involving only pure condensed phases and a gas phase, the equilibrium constant can be written solely in terms of those species which occur only in the gas phase.

By using T=298 K in Eq. (25), and by assuming the total pressure is equal to 1 and $P_{O_2} << 1$, $\Delta H_0$ and $\Delta G_T^\circ$ can be calculated.

Table 2 presents the Gibbs free energies and oxygen partial pressure for several possible reactions in the system.

Table 2: The possible reaction in the sintering system, the standard state Gibbs free energies of them and the required oxygen partial pressure of each reaction.

| | Reaction | $\Delta G_T^\circ$ | $P_{O_2}$ [atm] |
|---|---|---|---|
| 1 | $4Al_{(s)} + 3O_{2(g)} \rightarrow 2Al_2O_{3(s)}$ | $-3RT\ln(PO_2)$ | $4.5 \cdot 10^{-22}$ |
| 2 | $Al_4C_{3(s)} + 3O_{2(g)} \rightarrow 2Al_2O_{3(s)} + 3C_{(s)}$ | $-3RT\ln(PO_2)$ | $1 \cdot 10^{-18}$ |
| 3 | $2C_{(s)} + O_{2(g)} \rightarrow 2CO_{(g)}$ | $RT\ln(PO_2)$ | $1.8 \cdot 10^{-14}$ |
| 4 | $C_{(s)} + O_{2(g)} \rightarrow CO_{2(g)}$ | $RT\ln(PO_2)$ | $3.8 \cdot 10^{-11}$ |
| 5 | $2Al_2O_{3(s)} + 12CO_{2(g)} \rightarrow 4AlC_{3(s)} + 15O_{2(g)}$ | $-15RT\ln(PO_2)$ | $3.1 \cdot 10^{-9}$ |
| 6 | $2Al_2O_{3(s)} + 12C_{(s)} \rightarrow 4AlC_{3(s)} + 3O_{2(g)}$ | $3RT\ln(PO_2)$ | 0.14 |

According to the XRD, Raman spectroscopy, STEM-EDS and EELS results, stable alumina and crystalline graphite were formed in the sintered carbon doped alumina samples and carbon did not (completely) oxidize in the furnace. According to that, the oxygen partial pressure range was estimated to be $1.8 \cdot 10^{-14}$-$1 \cdot 10^{-18}$ atm.

## 5.2 The Influence of Carbon on Densification of Alumina

According to the reduction in the relative density with increasing in carbon amount (Table 1), the secondary carbon phase is believed to hinder densification, and result in the bimodal size distribution of alumina gains (Figure 8 (b)).

The annealing time required to reach a homogeneous carbon distribution in the alumina grains was estimated via [65]

$$t = \frac{\langle x \rangle^2}{2D} \tag{29}$$

where $t$ is the diffusion time, $\langle x \rangle$ is the average distance travelled by a diffusing particle in time t and D is the diffusion coefficient.

Guenette et al. estimated the carbon diffusion coefficients in alumina at different temperatures by examining elastic recoil detection analysis elemental depth profiles [66]. The diffusion coefficient of carbon in alumina at 1600°C can be estimated according to an alternative form of the Arrhenius equation [67]:

$$D = D_o \exp\left(\frac{-E_a}{RT}\right) \tag{30}$$

where $D_o$ is a constant and $E_a$ is the activation energy.

This results in a diffusion coefficient of $2.9 \cdot 10^{-13}$ $cm^2/s$ for carbon in alumina at 1600°C. Considering a final average grain size not larger than 1 µm, based on grain size measurements of carbon doped alumina samples done by Marder et al. (1 ± 0.2 µm after sintering 1600°C/ 2 h at the same conditions as in the present work), and based on the bimodal distribution of the

grain size which resulted in the "fully saturated carbon doped alumina" samples (and average grain sizes of 150 and 680 nm after sintering for 1600°C/ 6 h), 6 h of sintering time was chosen to ensure a homogenous carbon distribution.

The sintering environment itself (graphite furnace used in this study) does not result in a carbon content above the solubility limit, according to a similar density measurement for undoped alumina (sintered in air) and "gray alumina" (undoped alumina sintered in $CO/CO_2$ atmosphere). Miranzo et al. sintered alumina samples in $CO/CO_2$ environment and measured the resulted relative density, compared to conventional sintering in air [33]. Their samples sintered in a $CO/CO_2$ atmosphere reached 85% (the pre-sintered samples included an organic binder, which is an additional amount of carbon) and 88% (the organic binder was burned-out before sintering, similar to the "gray alumina" presented in this work). This is significantly lower than the conventional air-sintered alumina samples (99-99.5% relative density). According to Miranzo et al. the assumed oxygen partial pressure range was $10^{-15}$-$10^{-19}$ atm, similar to the oxygen partial pressure range used in the present work. However, their alumina powder includes several impurities, including Mg and Si at amounts which are above the solubility limit in alumina [14,24], so it might be that the presence of additional impurities together with carbon, hinders alumina densification.

Marder et al. sintered a ready-to-press (RTP) alumina, which contained Mg at a concentration above its solubility limit in alumina (but without Si) [32]. In contrast to Miranzo et al, Marder et al. reported on the same final relative density (~99%) for samples sintered both in air and in a $CO/CO_2$ atmosphere. Moreover, the carbon-environment sintered alumina sample resulted in a carbon content below the solubility limit. In separate experiments Marder et al. doped their RTP alumina with carbon to an estimated concentration of ~3 wt.%, which limited the density to ~97.5% in addition to reducing the grain size. Yahya et al. investigated the influence of a small amount of carbon (0.012 wt.%) on the fracture mode and abrasive wear resistance of alumina [30]. Similar to Marder et al, a carbon content below the solubility limit increased the alumina wear resistance. These results agree with the carbon content correlated to densification and grain growth findings in the present work. An increase in the final density is seen with higher sintering temperature and time. The “2% carbon doped alumina” samples sintered at 1600 °C/ 6 h resulted in 86% relative density. Annealing these samples at 1900°C/ 6 h and then 1600°C/ 6 h resulted in 96% relative density (Table 1). The increase in sintering temperature

and time resulted in an increase in the alumina grain size and coalescence of the graphite secondary phase (in Figure 9).

It has been shown that carbon segregates to alumina grain boundaries in 0.012 wt.% carbon doped alumina [31], as well as carbon adsorption to the triple junctions of alumina [32], probably driven by reduction of surface energy (i.e. Gibbsian adsorption). The driving force for densification during sintering is that the grain boundary energy is lower than the surface energy. However, if an adsorbed element reduces the surface energy to values below those of the grain boundary energy, the driving force for sintering is removed. If an additional bulk phase (above the solubility limit) forms a film on the surface of the grains and if this phase (e.g. graphite) has a lower surface energy than the alumina grain boundary energy, then again the driving force for sintering is eliminated. The alumina grain boundary energy range is 0.3-0.5 $J/m^2$ (assuming that the alumina grain boundary energy is some fraction of the alumina surface energy) [68,69], and the surface energy of graphite is 0.064 $J/ m^2$ [70]. Thus a graphite film on the surface of the alumina grains should hinder densification.

## 5.3 Carbon Content Measurements

### 5.3.1 Removal of Hydrocarbon Contamination

A WDS-based method for the measurement of carbon concentration was developed, by considering the hydrocarbon contamination, including efforts to reduce the amount of contamination in the system and samples via plasma etching and the use of oil-free pumps during the measurements.

The contamination rate was measured as a function of accelerating voltage to study hydrocarbon contamination as a function of electron beam energy (Figure 17). This showed a decrease in the contamination rate with increasing electron energy. At relatively low probe energies, most of the electron inelastic scattering in in a region that is very close to the sample surface, leading to an increased BSE and SE emission and contribution to hydrocarbon contamination. As the electron energy increases, fewer electrons will interact with the hydrocarbons on the surface, resulting in less contamination production. Figure 17 demonstrates that at ~12 kV contamination is minimized and remains constant with increasing energy. The electron beam energy used in this work is 10 kV, which is relatively close to the minimized contamination values seen in Figure 17.

### 5.3.2 Explanation of the Histogram Shape

In contrast to Mg, Ca and Si doped alumina [14,15,20,24], the WDS histogram for carbon doped alumina includes a gap between the low concentration range (solubility limit) and the high concentration range (secondary phase). This is due to the formation of graphite (pure carbon) as a secondary phase, compared to a compound, for example, $MgAl_2O_4$ for Mg-doped alumina. This allows the histogram to be used to estimate the size of the smallest graphite particles in the samples. According to the measured histogram (Figure 18), the lowest concentration in the higher concentration range is ~8067 ppm. After removing the carbon solute content (3940 ppm) and assuming a spherical graphite particle within the electron interaction volume at 10 kV, the smallest graphite particle should be ~119 nm in diameter.

### 5.3.3 Possible Errors in the ZAF Correction Applied in this Study

As explained before, the carbon content was measured from Au-coated samples (in order to prevent charging during the WDS measurements). In this study, Au coatings were used and not carbon coatings as used in the solubility limit measurements in the past [14,19,20,24,26]. In the present experiments carbon coatings cannot be used. Au was chosen as the coating element since a high purity (99.999%) source including in-situ plasma cleaning was available, in addition to the fact that the mass absorption coefficient of carbon-Kα ($1.52 \cdot 10^4$ $cm^2/g$) is of the same order of magnitude as for absorption of carbon in alumina ($1.72 \cdot 10^4$ $cm^2/g$) [71]. However, the graphite standard was not Au coated due to the significant change in the mass absorption of carbon-Kα in carbon ($2.35 \cdot 10^3$ $cm^2/g$) compared to absorption in Au.

The ZAF correction factor can only be applied to a single phase and not a mixture of phases, so the Au coating present on the alumina is not included in the ZAF correction. However, the presence of the Au coating can cause possible errors, that should be taken into account.

Reed considered X-ray intensity losses due to electron energy losses as [72]

$$\frac{I_0 - I}{I_0} = \frac{8.3 \cdot 10^5 \rho x}{E_0^2 - E_c^2} \tag{31}$$

where $I$ is the intensity measured from a coated sample, $I_0$ is the theoretical intensity without a coating, and $x$ is the coating thickness. According to this expression, the X-rays intensity losses due to electron energy losses within the Au coating (at 10 kV) reach 17%. However, according to Monte Carlo simulations using more physical cross-sections than were available during Reed's work (Figure 24) only 8% of the backscattered electrons will not be transmitted through a 10nm thick Au layer at 10 kV [73].

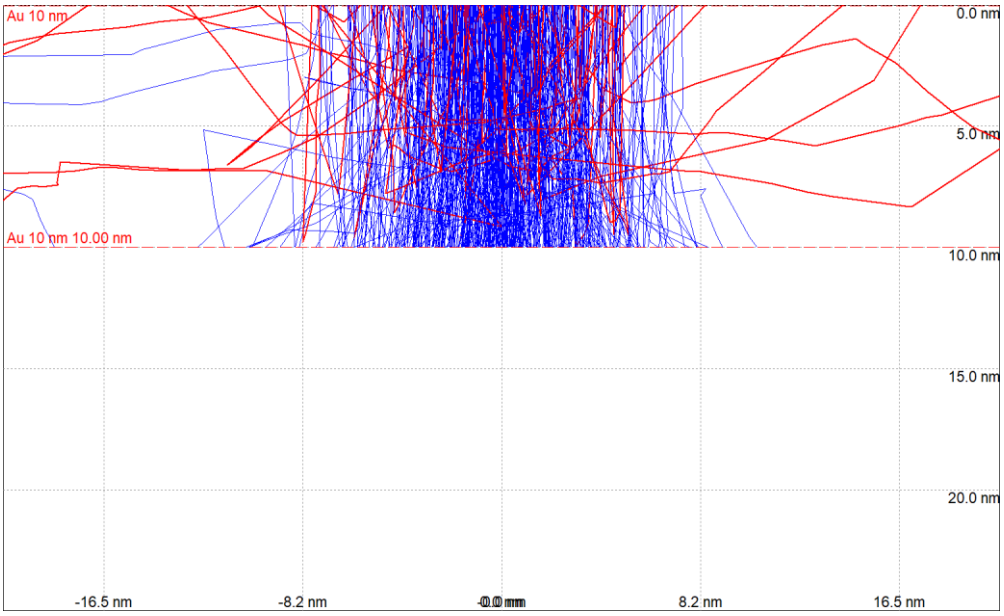


Figure 24: A Monte-Carlo simulation for 500 electron trajectories through Au assuming 10 kV incident beam. The trajectories in red indicate backscattered electrons that eventually escape from the surface of the sample. The simulation was calculated using the software program Casino [73].

The coating material may also fluorescence the element of interest, resulting in an increased X-ray signal which must be considered. The fluorescence correction factor can be expressed as [74,75]:

$$\frac{I_F}{I_0} = 0.5 c_{coat} \frac{\left(\mu/\rho\right)_{coat}^{coat}}{\left(\mu/\rho\right)_{matrix}} \frac{r_K - 1}{r_K} \omega_k \frac{M}{M_{coat}} \frac{\left(U_{coat}\ln(U_{coat}) - U_{coat} + 1\right)}{\left(U\ln(U) - U + 1\right)} \qquad (32)$$

where $I_F$ is X-ray intensity due to fluorescence, $\frac{r_K - 1}{r_K}$ is the absorption edge jump ratio of the K shell of the element of interest, $\omega_k$ is the fluorescence yield of the K shell X-rays photons and $U_i$ is equals to $E_0/E_c$.

In order to estimate the Au content ($c_{coat}$), the amount of Au under the incident beam (conservatively estimated to be 500 nm in diameter) was considered to be "dissolved" in the X-ray interaction volume of the alumina matrix (604 nm in diameter according to Eq.(17)) as schematically presented in Figure 25.

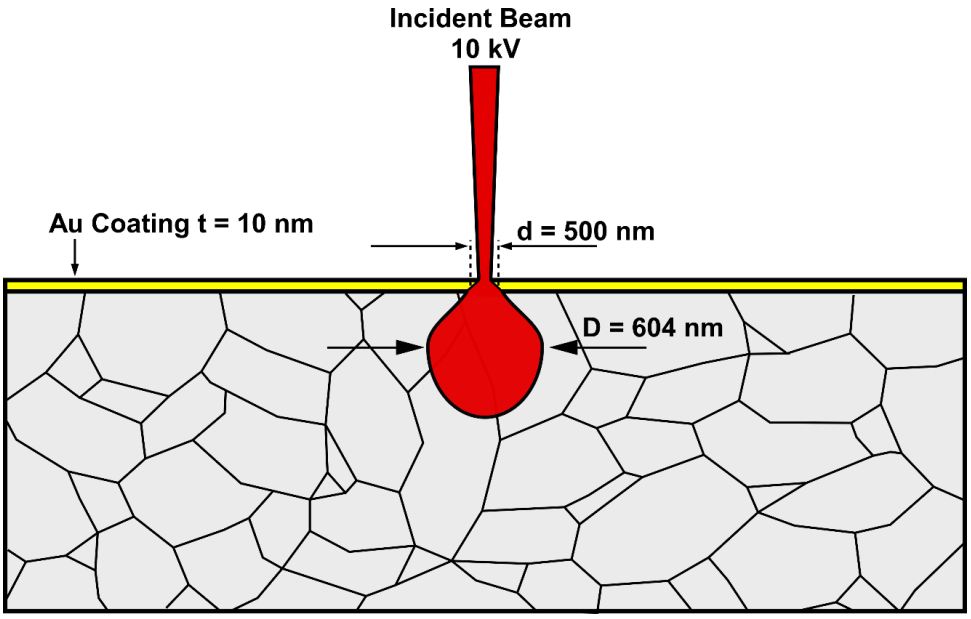


Figure 25: A schematic drawing of the interaction volume in alumina under a 10 nm thick Au coating. A conservatively large beam diameter of 500nm was used to estimate the total number of Au atoms hypothetically dissolved in the interaction volume. From this the possible influence of Au fluorescence was estimated.

The Au content in this volume would define a concentration of 1.65 wt.%, leading to an increase carbon intensity due to fluorescence ~0.0002 %, which is insignificant.

In addition, the Au coating will change the mass–thickness depth distribution for X-ray generation, which in turn will affect the subsequent emission. Due to the higher density of Au ($\rho_{Au}$=19.32 g/cm$^{3)}$ compared to alumina ($\rho_{alumina}$=3.98 g/cm$^{3)}$, the presence of a Au coating on the alumina will shift the mass–thickness depth distribution of the X-rays closer to the surface, as shown in the Monto-Carlo simulations presented in Figure 26.

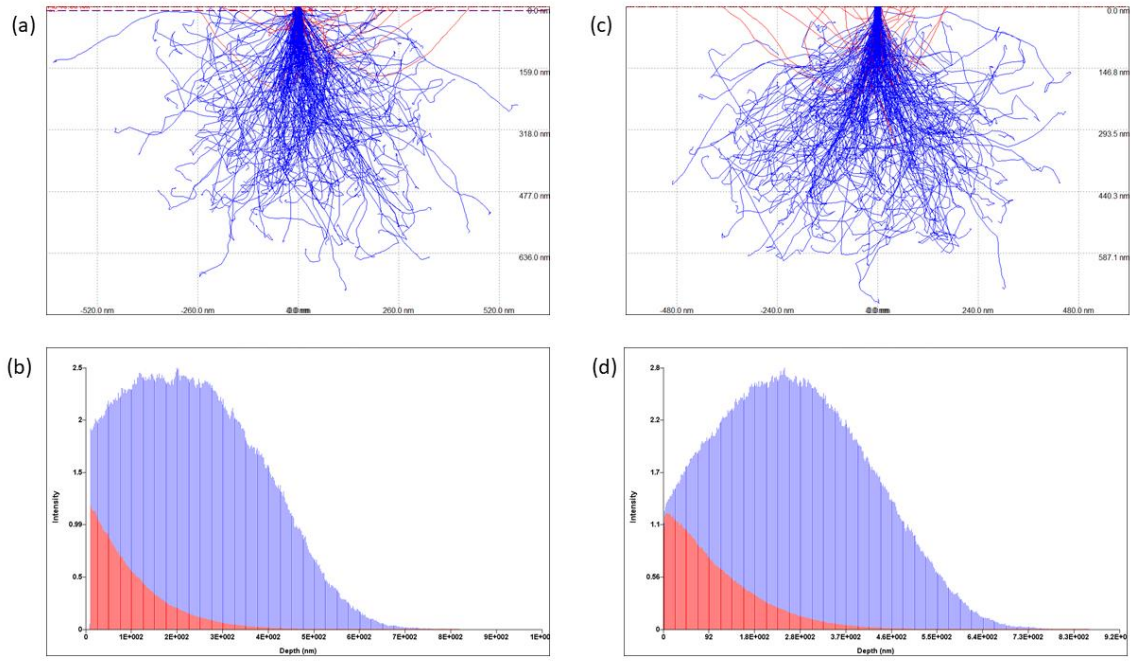


Figure 26: A Monte-Carlo simulation for 500 electron trajectories at 10 kV incident energy through (a) alumina with a 10 nm Au coating and (c) alumina without a coating, and the carbon-Kα distribution in (b) Au coated alumina and (d) non-coated alumina. The distributions are separated to absorbed (red) and non- absorbed (blue) carbon- Kα [73].

The most important aspect of this effect is X-ray absorption during emission from the sample. If the depth distribution is shallower, the absorption of photons during emission will be less. Accordingly, the presence of a Au coating decreases absorption, resulting in a higher X-ray intensity compared to the non-coated alumina. In the case of carbon-Kα, which has high absorption, this phenomenon cannot be ignored. Note that the difference in the mass absorption coefficients of carbon-Kα in alumina and Au can be ignored since they are of the same order of magnitude [71].

Therefore, we expect the carbon X-ray signal to be higher in the presence of Au coating, and therefore the carbon concentration (in this case the solubility limit) will be smaller than the one determined using the standard ZAF correction. Unfortunately, there is no current model to fully modify ZAF correction factor to take this into account.

However, we can try to determine the solubility limit of carbon in alumina from the measured X-rays intensities with a Au coating where we computationally dissolve the relevant volume of the Au film into the interaction volume of the alumina (1.65 wt.% for this work), in addition to

the carbon. Using this approach, the solubility limit of carbon in alumina would be 3940 ± 906 ppm; 189 ppm less than that determined using an uncorrected ZAF.

Finally, it should be noted that the carbon doped alumina samples were furnace-cooled at a rate of ~60°C/min. This cooling rate may be too slow to prevent carbon diffusion, and since the solubility limit of carbon in alumina is expected to decrease with decreasing temperature, during furnace-cooling the solute content of the alumina grains may decrease until a temperature is reached where bulk diffusion becomes insignificant. In the case of Ca in alumina, this temperature was shown to be ~1300°C [32]. Thus 3940 ppm represents the carbon solubility limit at some temperature below 1600°C.

## 5.4 The High-Temperature Solubility Limit of Mg in Alumina

The solubility limit of Mg in alumina at the relatively low oxygen partial pressure used in this study is 166± 42 ppm, at 1600°C. According to Miller et al. the solubility limit of Mg in alumina in air at 1600°C is 132 ppm [14]. According to Futazuka et al., the solubility limit of group IIA (including Mg and Ca) should not be significantly affected by the oxygen partial pressure [41]. In the case of Mg, the point defects mechanism in Mg doped alumina system is reported to be the same for high and low oxygen partial pressures, which is Al substitution by Mg cations and Mg interstitials, both charged compensated via oxygen vacancies [10,41].

The sintering environment used to prepare the Mg doped alumina samples was a graphite furnace. Before sintering, the Mg doped alumina samples were annealed in air at 1600°C for 2 h in order to start the densification process without the presence of graphite, in order to minimize the amount of carbon that can dissolve into the samples during sintering. According to the Raman results, the Mg doped alumina samples did not contain a secondary carbon phase, which means carbon below its solubility limit in alumina. According to the WDS measurements, the carbon content in the Mg doped alumina samples was ~1500 ppm.

The influence of Mg on the solubility limit of carbon in alumina needs to be studied. In the case of Mg and Ca co-doped alumina, Mg was found to reduce the solubility limit of Ca from 51 to 32 ppm at 1600°C, suggesting that the increased Mg in solution results in more Mg excess at the alumina grain boundaries, thus contributing to a decreased grain boundary mobility by solute drag [26].

It should be noted that the Mg doped alumina samples were Au coated. The mass absorption of Mg-Kα in alumina ($1.53 \cdot 10^3$ $cm^2/g$) is similar to its absorption in Au ($3.23 \cdot 10^3$ $cm^2/g$) [71]. The fluorescence of the Mg-Kα by Au was calculated to be ~0.025% (Eq.(32)) and can be ignored. As was done for the carbon content analysis, the correction for ZAF can estimated by computationally adding Au as a solute for the ZAF calculations. According to that, the solubility limit of Mg in alumina would be 171 ppm; only a 5 ppm difference from the determined value using an uncorrected ZAF.

In addition, the Mg doped alumina samples were furnace-cooled at a rate of ~60°C/min, meaning that the determinate value represents the Mg solubility limit at some temperature below 1600°C at a low oxygen partial pressure.

# 6. Summary and Conclusions

Pure (99.99%) polycrystalline alumina was doped with carbon at concentrations which were confirmed to be above the solubility limit. The secondary phase was confirmed to be graphite by Raman and S/TEM-EELS, and it is believed to hinder densification of alumina during sintering. Undoped alumina which was sintered in air was used to measure the carbon signal due to hydrocarbon contamination in the SEM chamber, and these values were subtracted as a background signal from the carbon doped alumina samples.

The carbon content of the saturated alumina grains, equilibrated at 1600°C, was determined by WDS to be 3940± 906 ppm with a detection limit of 15 ppm, and it is believed that carbon substitutes oxygen as an anion and this is charge-compensated by the formation of oxygen vacancies. This result shows that carbon has a significant solubility in bulk alumina under low oxygen partial pressures found in graphite-based furnaces. The WDS-based method of quantifying the actual carbon content in bulk alumina can be useful in correlating its influence on the microstructural evolution of alumina.

In addition, the solubility limit of Mg in alumina at 1600°C relatively low oxygen partial pressure was determined by WDS to be 166± 42 ppm with a detection limit of 3 ppm.

.

# 7. Recommendations for Future Work

The goal of this research was to study the high-temperature solubility limit of carbon in alumina. This was accomplished by a WDS-based method that took hydrocarbon contamination into account. However, the solubility limit measurements were done on Au-coated samples, which at this point can't be fully considered in the standard ZAF correction factor. From Monte Carlo simulations of electron scattering it was concluded that Au shifts the mass-thickness distribution for X-ray generation closer to the surface, thus decreasing the path for exiting X-rays, and the amount of absorption is thus less. A model which can calculate the change in the X-rays depth profile is needed to understand the full influence of a conductive (Au) coating on the determined solubility limit.

The magnitude of the Au coating on the mass-thickness distribution of the X-ray signal could be evaluated by conducting additional experiments on the solubility limit of Mg in alumina. The original WDS measurements were conducted on carbon coated samples, resulting in a solubility limit of 132 ppm (in air). By preparing similar alumina samples and coating them with Au, the magnitude of the influence of the Au film could be evaluated.

A corroboration of the measured solubility limit should be done via another experimental method. This requires high spatial resolution and a fully quantitative approach. We have tried to use secondary ion mass spectroscopy (SIMS) in order to measure the carbon content, however the matrix effects required a similar standard to be measured in order to determine a quantitative value. No standards are available, except by ion implantation which requires simulations to estimate the actual carbon distribution, and this approach really would not corroborate the present findings.

A possible quantitative measurement could be done by X-ray fluorescence (XRF). The XRF technique does not require a conductive coating due to the photon source, so the amount of carbon can be measured directly from the alumina. However, the spatial resolution of XRF is not good enough to measure a solute in a two phase system (it will always interact with the secondary phase). Therefore, the measurement needs to be done on a one phase system. XRF is usually done in air; , a higher hydrocarbon-contaminated environment. We propose to mount a copper foil below the SEM column (in the vacuum chamber), and to use the incident electron

beam to generate Cu photons for irradiation of the sample. In this way the existing EDS and WDS detectors can be used to measure the XRF signal, and for samples doped below the solubility limit this can be used to corroborate the quantitative WDS analysis which was used here.

After determination of the solubility limit of carbon and Mg in alumina at low oxygen partial pressure, the influence of Mg on the solubility limit of carbon (and vice versa) should be studied by WDS measurements on a co-doped alumina system.

# 8. References


1. S. J. L. Kang. Sintering: Densification, Grain Growth and Microstructure. Elsevier Science, 2005, p 7-9.
2. A. D. McNaught, A. Wilkinson, Compendium of Chemical Terminology, (the "Gold Book"), Oxford, 1997.
3. M. N. Rahaman, Sintering of Ceramics, CRC Press, p 580-582, 2008.
4. J.W. Cahn, The impurity-drag effect in grain boundary motion, Acta Metallurgica, 10[9]: 789–798, 1962.
5. J.D. Powers, A.M. Glaeser, Grain Boundary Migration in Ceramics, Interface Science, 6[1]: 23–39, 1998.
6. I. Levin, D. Brandon, Metastable Alumina Polymorphs: Crystal Structures and Transition Sequences, Journal of the American Ceramic Society, 81[8]: 1995–2012, 1998.
7. M. L. Kronberg, Plastic Deformation of Single Crystals of Sapphire: Basal Slip and Twinning, Acta Metallurgica, 5[9]: 507–524, 1957.
8. D. Brandon, W.D. Kaplan, Microstructural Characterization of Materials, John Wiley & Sons, Ltd, 2008.
9. R. L. Coble. Transparent Alumina and Method of Preparation. US Patent Office US3026210A, 1962.
10. W.C Johnson, R. L Coble, A Test of the Second-Phase and Impurity-Segregation Models for MgO-Enhanced Densification of Sintered Alumina, Journal of the American Ceramic Society, 61[3-4] 110–114, 1978.
11. S.K. Roy, R.L. Coble, Solubilities of Magnesia, Titania, and Magnesium Titanate in Aluminum Oxide, Journal of the American Ceramic Society. 51[1]: 1–6, 1968.
12. J. Rödel, A.M. Glaeser, Anisotropy of Grain Growth in Alumina. Journal of the American Ceramic Society, 73[11]: 3292-3301, 1990.
13. B. Hallstedt, Thermodynamic Assessment of the System MgO–$Al_2O_3$, Journal of the American Ceramic Society, 75[6]: 1497–1507, 1992.
14. L. Miller, A. Avishai, W.D. Kaplan, Solubility Limit of MgO in $Al_2O_3$ at 1600°C, Journal of the American Ceramic Society. 89[1]: 350–353, 2006.
15. R. Akiva, A. Katsman, W.D. Kaplan, Anisotropic Grain Boundary Mobility in Undoped and Doped Alumina, Journal of the American Ceramic Society, 97[5]: 1610–1618, 2014.
16 C. A. Handwerker, P. A. Morris, R. L. Coble, Effects of Chemical Inhomogeneities on Grain Growth and Microstructure in $Al_2O_3$, Journal of the American Ceramic Society, 72[1]: 130-136, 1989.
17. S. J. Dillon, M. P. Harmer, Relating Grain-Boundary Complexion to Grain-Boundary Kinetics I: Calcia-Doped Alumina, Journal of the American Ceramic Society, 91[7]: 2304-2313, 2008.
18. Kenneth A. McGowan, Calcium aluminate clinker as a refractory aggregate with and without barium addition and use thereof, US Patent Office 8123853 B2, 2012.

19. R. Akiva, A. Berner, W.D. Kaplan, The Solubility Limit of CaO in α-Alumina at 1600°C, Journal of the American Ceramic Society, 96[10]: 3258–3264, 2013.

20. P. Ghosh, R. Marder, A. Berner, W.D. Kaplan, The influence of temperature on the solubility limit of Ca in alumina, Journal of the European Ceramic Society, 40[15]: 5767–5772, 2020.

21. S.I. Bae, S. Baik, Determination of Critical Concentrations of Silica and/or Calcia for Abnormal Grain Growth in Alumina, Journal of the American Ceramic Society, 76[4]: 1065–1067, 1993.

22. S.J. Dillon, M.P. Harmer, Relating Grain Boundary Complexion to Grain Boundary Kinetics II: Silica-Doped Alumina, Journal of the American Ceramic Society, 91[7]: 2314–2320, 2008.

23. F.J. Klug, S. Prochazka, R.H. Doremus, Alumina-Silica Phase Diagram in the Mollite Region, Journal of the American Ceramic Society, 70[10]: 750–759, 1987.

24. R. Moshe, A. Berner, W.D. Kaplan, The solubility limit of $SiO_2$ in α-alumina at 1600°C, Scripta Materialia, [86]: 40–43, 2014.

25. C.A. Handwerker, P.A. Morris, R.L. Coble, Effects of Chemical Inhomogeneities on Grain Growth and Microstructure in Al2O3, Journal of the American Ceramic Society, 72[1]: 130–136, 1989.

26. R. Moshe, W.D. Kaplan, The combined influence of Mg and Ca on microstructural evolution of alumina, Journal of the American Ceramic Society, 102[8]: 4882–4887, 2019.

27. K. Morita, B. N. Kim, H. Yoshida, K. Hiraga, Y. Sakka, Distribution of carbon contamination in oxide ceramics occurring during spark-plasma-sintering (SPS) processing: II – Effect of SPS and loading temperatures, Journal of the European Ceramic Society, 38[6]: 2596–2604, 2018.

28. M. Biesuz, V.M. Sglavo, Flash sintering of alumina: Effect of different operating conditions on densification, Journal of the European Ceramic Society, 36[10]: 2535–2542, 2016.

29. M. Michálek, M. Michálková, G. Blugan, J. Kuebler, Effect of carbon contamination on the sintering of alumina ceramics, Journal of the European Ceramic Society, 38[1]: 193–199, 2018.

30. N.A. Yahya, R.I. Todd, Influence of C doping on the fracture mode and abrasive wear of $_{Al2O3}$, Journal of the European Ceramic Society, 32[16] 4003–4007, 2012.

31. E.A. Marquis, N.A. Yahya, D.J. Larson, M.K. Miller, R.I. Todd, Probing the improbable: Imaging C atoms in alumina, Materials Today, 13[10]: 34–36, 2010.

32. R. Marder, P. Ghosh, I. Reimanis, W.D. Kaplan, The Influence of Carbon on the Microstructure and Wear Resistance of Alumina, Journal of the American Ceramic Society, 104[8]: 4214-4225, 2021.

33. P. Miranzo, L. Tabernero, J.S. Moya, J.R. Jurado, Effect of Sintering Atmosphere on the Densification and Electrical Properties of Alumina, Journal of the American Ceramic Society, 73[7]: 2119–2121, 1990.

34. I. Ahmad, H. Cao, H. Chen, H. Zhao, A. Kennedy, Y.Q. Zhu, Carbon nanotube toughened aluminum oxide nanocomposite, Journal of the European Ceramic Society, 30[4]: 865–873, 2010.

35. K. H. Lee, J. H. Crawford Jr., Additive coloration of sapphire, Applied Physics Letters, [33]: 273–275, 1978.

36. M.S. Akselrod, V.S. Kortov, D.J. Kravetsky, V.I. Gotlib, Highly Sensitive Thermoluminescent Anion-Defective Alpha-$Al_2O_3$:C Single Crystal Detectors, Radiation Protection Dosimetry, 32[1]: 15–20, 1990.

37. V. Kortov, I. Milman, Some New Data on Thermoluminescence Properties of Dosimetric Alpha-$Al_2O_3$ Crystals, Radiat, Radiation Protection Dosimetry, 65[1-4]: 179–184, 1996.

38. E.G. Yukihara, B.A. Doull, M. Ahmed, S. Brons, T. Tessonnier, O. Jäkel, S. Greilich, Time-resolved optically stimulated luminescence of $Al_2O3$:C for ion beam therapy dosimetry, Physics in Medicine & Biology, [60]: 6613–6638, 2015.

39. X.-B. Yang, H.-J. Li, Q.-Y. Bi, Y. Cheng, Q. Tang, J. Xu, Influence of carbon on the thermoluminescence and optically stimulated luminescence of α-Al2O3:C crystals, Journal of Applied Physics, [104]: 123112, 2008.

40. J. Zhu, K.P. Muthe, R. Pandey, Stability and electronic properties of carbon in α-$Al_2O_3$, Journal of Physics and Chemistry of Solids, 75[3]: 379–383, 2014.

41. T. Futazuka, R. Ishikawa, N. Shibata, Y. Ikuhara, First-principles calculations of group IIA and group IV impurities in α- $Al_2O_3$, Physical Review Materials, 4[7]: 73602, 2020.

42. V.D. Scott, G. Love, and S.J.B. Reed, Quantitative Electron-Probe Microanalysis, Ellis Horwood, New York, 1995, p. 19–59, 93–107.

43. A. Berner, F. Gimelfarb, and T. Ukhorskaya, Metrological Aspects of Microprobe Analysis, Journal of Analytical Chemistry (Russian), 37[2]: 338–48, 1982.

44. A.E. Vladár, K.P. Purushotham, M.T. Postek, Contamination specification for dimensional metrology SEMs, Proc.SPIE, 6922: 692217-5, 2008.

45. L. Reimer, Scanning Electron Microscopy, Springer Series in Optical Sciences, 1998.

46. M.T. Postek, An approach to the reduction of hydrocarbon contamination in the scanning electron microscope, Scanning, 18[4]: 269–274, 1996.

47. G.W. Hollenberg, R.S. Gordon, Effect of Oxygen Partial Pressure on the Creep of Polycrystalline $Al_2O_3$ Doped with Cr, Fe, or Ti, Journal of the American Ceramic Society, 56[3]: 140–147, 1973.

48. R.S. Krishnan, Raman Spectrum of Alumina and the Luminescence and Absorption Spectra of Ruby, Nature, 160: 26–26, 1947.

49. A.C. Ferrari, J. Robertson, Interpretation of Raman spectra of disordered and amorphous carbon, Physical Review B, 61: 14095–14107, 2000.

50. A.C. Ferrari, Raman spectroscopy of graphene and graphite: Disorder, electron–phonon coupling, doping and nonadiabatic effects, Solid State Communications, 143[1-2]: 47–57, 2007.

51. F. Tuinstra, J.L. Koenig, Raman Spectrum of Graphite, The Journal of Chemical Physics, 53[3]:1126–1130, 1970.

52. H. Wilhelm, M. Lelaurain, E. McRae, B. Humbert, Raman spectroscopic studies on well-defined carbonaceous materials of strong two-dimensional character, Journal of Applied Physics, 84[12]: 6552–6558, 1998.

53. P. Ewels, T. Sikora, V. Serin, C.P. Ewels, L. Lajaunie, A Complete Overhaul of the Electron Energy-Loss Spectroscopy and X-Ray Absorption Spectroscopy Database: eelsdb.eu, Microscopy and Microanalysis, 22[3]: 717–724, 2016.

54. C.C. Ahn, O.L. Krivanek, EELS Atlas : a reference collection of electron energy loss spectra covering all stable elements, Gatan, Warrendale, PA, 1983.

55. H. Cynn, S.K. Sharma, T.F. Cooney, M. Nicol, High-temperature Raman investigation of order-disorder behavior in the $MgA1_2O_4$ spinel, Physical Review B, 45[1]: 500–502, 1992.

56. X.-B. Yang, H.-J. Li, Q.-Y. Bi, Y. Cheng, Q. Tang, J. Xu, Influence of carbon on the thermoluminescence and optically stimulated luminescence of α-$Al_2O_3$:C crystals, Journal of Applied Physics, 104[12]: 123112, 2008.

57. M.S. Akselrod, V.S. Kortov, D.J. Kravetsky, V.I. Gotlib, Highly Sensitive Thermoluminescent Anion-Defective Alpha-$Al_2O_3$:C Single Crystal Detectors, Radiation Protection Dosimetry, 32[1]: 15–20, 1990.

58. S.U. Khan, M. Al-Shahry, W.B. Ingler Jr., Efficient Photochemical Water Splitting by a Chemically Modified n-$TiO_2$, Science, 297 [5590]: 2243–2245, 2002.

59. S. Seo, T. Nam, H.-B.-R. Lee, H. Kim, B. Shong, Molecular oxidation of surface $–CH_3$ during atomic layer deposition of $Al_2O_3$ with $H_2O$, $H_2O_2$, and $O_3$: A theoretical study, Applied Surface Science, 457: 376–380, 2018.

60. A.C. Dillon, A.W. Ott, J.D. Way, S.M. George, Surface chemistry of $Al_2O_3$ deposition using $Al(CH_3)_3$ and $H_2O$ in a binary reaction sequence, Surface Science, 322[1-3]: 230–242, 1995.

61. C. Zener, Relation between residual strain energy and elastic moduli, Acta Crystallographica, 2: 163–166, 1949.

62. D.B. Hovis, A. Reddy, A.H. Heuer, X-ray elastic constants for α-$Al_2O_3$, Applied Physics Letters, 88[13]: 131910, 2006.

63. Handbook of Chemistry and Physics, 60th Edition, Ed. Robert C. Weast, CRC Press Inc., Boca Raton, Florida, 1979.

64. Gaskell, David R. Introduction to the Thermodynamics of Materials. CRC press, 2012. p 419-420.

65. P. Atkins and Julio de Paula, Physical Chemistry, Ninth Edition, Great Britain by Oxford University Press, 2010.

66. M.C. Guenette, M.D. Tucker, M. Ionescu, M.M.M. Bilek, D.R. McKenzie, Carbon diffusion in alumina from carbon and $Ti_2AlC$ thin films, Journal of Applied Physics, 109[8]: 83503, 2011.

67. D.R Askeland, Atom Movement in Materials. In: The Science and Engineering of Materials. Springer, Boston, MA, 1996.

68. G. Gluzer, W.D. Kaplan, Particle occlusion and mechanical properties of Ni–$Al_2O_3$ nanocomposites, Journal of the European Ceramic Society, 33[15-16]: 3101–3113, 2013

69. J.D. Powers, A.M. Glaeser, Grain Boundary Migration in Ceramics, Interface Science, 6: 23–39, 1998.

70. J. Lee, B. Lee, A simple method to determine the surface energy of graphite, Carbon letters, 21: 107–110, 2017.

71. B.L. Henke, P. Lee, T.J. Tanaka, R.L. Shimabukuro, B.K. Fujikawa, Low-energy x-ray interaction coefficients: Photoabsorption, scattering, and reflection: E = 100–2000 eV Z = 1–94, Atomic Data and Nuclear Data Tables, 27[1]: 1–144, 1982.

72. S. J. B. Reed, Electron Microprobe Analysis, Department of Mineralogy and Petrology, University of Cambridge, 1975, p 180

73. D. Drouin, A.R. Couture, D. Joly, X. Tastet, V. Aimez, R. Gauvin, CASINO V2.42—A Fast and Easy-to-use Modeling Tool for Scanning Electron Microscopy and Microanalysis Users, Scanning, 29[3]: 92–101, 2007.

74. S.J.B. Reed, Characteristic fluorescence corrections in electron-probe microanalysis, Br. British Journal of Applied Physics, 16: 913–926, 1965.

75. M.O. Krause, Atomic radiative and radiationless yields for K and L shells, Journal of Physical and Chemical Reference Data, 8[2]: 307–327, 1979.

# גבול המסיסות של פחמן באלומינה בטמפרטורה גבוהה

לי-אור כהן

# גבול המסיסות של פחמן באלומינה בטמפרטורה גבוהה

חיבור על מחקר

לשם מילוי חלקי של הדרישות לקבלת התואר

מגיסטר למדעים בהנדסת חומרים

**לי-אור כהן**

הוגש לסנט הטכניון – מכון טכנולוגי לישראל

טבת תשפ"ב חיפה ינואר 2022

# תודות

אני מודה לטכניון על חלקו בתמיכה הכספית בהשתלמותי. מחקר זה נתמך בחלקו על ידי הקרן הלאומית למדע (מענק מספר 1779/18).

מחקר זה נערך בהנחיית פרופ' וויין ד. קפלן מהפקולטה למדע והנדסה של חומרים בטכניון – מכון טכנולוגי לישראל.

ברצוני להודות לפרופ' ווין קפלן על ההשראה, הסבלנות והעידוד המתמיד .

ברצוני להוקיר תודה לד"ר אלכס ברנר על דיון מעורר מחשבה, עזרה והכוונה .

תודה לחברי הפקולטה ולעמיתיי בקבוצת המחקר קרמיקה ומשטחי ביניים על תמיכתם .

תודה רבה למשפחתי על העידוד, האהבה והתמיכה.

# תקציר

תהליך הייצור של חומרים קרמיים נעשה על ידי סנטור. בסנטור מתחילים מאבקה דחוסה/ גוף ירוק ועל ידי טיפול תרמי בטמפרטורה גבוהה מתקבל מעבר מסה. במהלך הסנטור מתרחשים במקביל תהליכי הצטופפות וגידול גרעינים. הכוח המניע להצטופפות הינו הורדת אנרגית פני השטח על ידי החלפת פני שטח חופשיים בגבולות גרעין, להם אנרגיה נמוכה יותר בהשוואה לזו של פני השטח. גידול גרעינים מונע הודות להורדה של סך כל פני השטח במערכת. היות ושני תהליכים אלו מתרחשים בו זמנית, השליטה בהם הינה אחד מהאתגרים הגדולים שקיימים בתהליך הייצור של חומרים קרמיים.

אחת הדרכים בהן ניתן לשלוט בתהליכי הסנטור (או לשנותם) הינה על ידי סימום. קיימים שני מנגנונים אפשריים במערכת קרמית מסוממת, כתלות בכמות הסמם בה. כאשר כמות הסמם הינה מתחת לגבול המסיסות בחומר הקרמי מתקבלת סגרגציה בשיווי משקל של הסמם אל גבולות הגרעינים, במצבים בהם הוא גורם להורדה של אנרגית גבול הגרעין. באפקט Solute drag קלאסי הסמם מעכב את תנועת גבול הגרעין וישנם סממים שגורמים לתופעה הפוכה של האצת התנועה של גבול הגרעין. כאשר כמות הסמם הינה מעל גבול המסיסות, מתקבל התבדלות של הדופנט כפאזה משנית בהתאם לדיאגרמת פאזות. חלקיקי הפאזה המשנית מעכבים את תנועת גבול הגרעין ובכך מתקבלת תופעת Zener drag במערכת וגידול הגרעינים מעוכב. כל מנגנון משפיע אחרת על המיקרו-מבנה של החומר הקרמי וכתוצאה מכך גם על תכונותיו, על כן חשוב לדעת מהו גבול המסיסות של סמם מסוים במערכת נתונה.

אלומינה היא אחת מהחומרים הקרמיים המרכזים במחקר ובתעשייה. סנטור אלומינה נעשה בדרך כלל באוויר, אולם מספר טכניקות סנטור חדשות הדורשות הגנה מפני חמצון והולכה חשמלית גבוהה (למשל SPS) מתבצעות באווירת גרפיט. על פי מחקרים רבים נמצא כי הפחמן מתמוסס בתוך האלומינה בעת תהליך הסנטור וגורם לשינוי המיקרו-מבנה ותכונות האלומינה. עם זאת, רוב המחקרים בעבר לא מדדו בפועל את ריכוז הפחמן המתקבל בדגם וגבול המסיסות שלו באלומינה טרם נקבע.

במחקר זה פותחה שיטה למדידת גבול המסיסות של פחמן באלומינה באמצעות מדידות ספקטרוסקופיה של פיזור גל (WDS) במיקרוסקופ אלקטרונים סורק (SEM). האתגר הגדול במדידת כמות פחמן במיקרוסקופ אלקטרונים הינה זיהומי הפחמימנים הנוצרים על פני שטח הדגם כתוצאה מאינטראקציה בין קרן האלקטרונים לבין מולקולות פחמימניות הספוחות לפני השטח. על מנת לקחת כמות זו בחשבון ולהסיר אותה מכמות הפחמן הנמדדת באלומינה, הוכן דגם אלומינה נקייה (שלא מכיל פחמן) אשר סונטר ב-1600°C למשך שעתיים באוויר וממנו נמדדה כמות הפחמימנים הנספחים לפני שטח הדגם במיקרוסקופ אלקטרונים. נעשה שימוש במשאבה ללא שמן במהלך המדידות ובכל יום מדידה בוצע ניקוי של הדגמים ושל תא המיקרוסקופ טרם המדידות, על מנת להוריד את כמות הזיהומים עד כמה שניתן. זיהומי הפחמן נמדדו בכל יום מדידה והוסרו מהמדידות שנלקחו מהדגם המכיל פחמן, אשר הוכן על ידי אינפילטרציה של גוף ירוק במי

גלוקוז ולאחר מכן עבר סנטור ב-1600°C למשך 6 שעות באווירת He בתנור גרפיט (המכנה לחץ חלקי נמוך) וקירור מהיר של כ-60°C בדקה. גבול המסיסות של פחמן באלומינה ב-1600°C שהתקבל הינו 906 ppm ± 3940 עם סף גילוי של 15 ppm. על פי מחקרים קודמים הכוללים חישובי DFT, בלחץ החלקי הנמוך מנגנון הפגמים הנקודתיים במערכת אלומינה-פחמן הוא החלפת חמצן על ידי אניון של פחמן, תוך הופעת היעדרות חמצן.

על סמך מדידות הצפיפות שנעשו עבור דגמי אלומינה עם ריכוזים שונים של פחמן מתקבל הרושם שכמות פחמן גבוהה גורמת לעיכוב/ מניעה של הצטופפות האלומינה. נמדד בעבר כי פחמן עובר סגרגציה לגבול הגרעין, כנראה בעקבות הורדה של אנרגית פני שטח. אם האלמנט הנספג מפחית את אנרגיית פני השטח לערכים מתחת לאלה של אנרגיית גבול הגרעין, הכוח המניע לסנטור יוסר. אם פאזה נוספת במטריצה (מעל גבול המסיסות) יוצרת שכבה על פני שטח הגרעינים, ואם לפאזה זו (למשל גרפיט) יש אנרגיית פני השטח נמוכה יותר מאנרגיית גבול הגרעין של גרעיני האלומינה, אז שוב הכוח המניע לסנטור מתבטל. אנרגיית גבול הגרעין של גרעיני האלומינה היא הינה בטווח של $0.3\text{-}0.5\ J/m^2$ ואנרגיית פני השטח של גרפיט הינה $0.064\ J/m^2$. לפיכך, שכבת הגרפיט על פני השטח של גרעיני האלומינה צפוי לעכב צפיפות, כפי שהתקבל במחקר הנוכחי.

בנוסף, על מנת להבין את השפעת אווירת הסנטור על גבול המסיסות באלומינה, נמדד גבול המסיסות של Mg באלומינה ב-1600°C בלחץ חלקי נמוך, בתנור גרפיטי באווירת הליום. על מנת למנוע מפחמן להתמוסס בדגם במהלך הסנטור, הדגמים הרווים במגנזיום עברו סנטור לצפיפות מלאה ב-1600°C באוויר. גבול המסיסות של Mg באלומניה בלחץ חלקי נמוך וב-1600°C הינו 42 ppm ± 166 בסף גילוי של 3 ppm. גבול המסיסות של Mg באלומינה באותה טמפרטורה באוויר הינו 132 ppm. ההנחה ללחץ החלקי לא תהיה השפעה רבה על גבול המסיסות של Mg באלומינה על פי סימולציות DFT.

כל מדידות ה-WDS נעשו כאשר הדגמים מצופים בציפוי זהב בעובי 10 nm, על מנת למנוע טעינה במהלך המדידות. במסגרת המחקר נחקרו שגיאות אפשרויות בחישוב פקטור תיקון ה-ZAF עבור המערכת שלנו בעקבות ציפוי הזהב.